2002

A survey of various frequency domain integral equations for the analysis of scattering from three-dimensional dielectric objects

Baek Ho Jung
Hoseo University

T. K. Sarkar
Syracuse University

Y.-S. Chung
Syracuse University

Progress In Electromagnetics Research, PIER 36, 193–246, 2002

A SURVEY OF VARIOUS FREQUENCY DOMAIN INTEGRAL EQUATIONS FOR THE ANALYSIS OF SCATTERING FROM THREE-DIMENSIONAL DIELECTRIC OBJECTS

B. H. Jung

Department of Information and Communication Engineering
Hoseo University
Asan 336-795, Korea

T. K. Sarkar and Y.-S. Chung

Department of Electrical Engineering and Computer Science
Syracuse University
Syracuse, NY 13244, USA

Abstract—In this paper, we present four different formulations for the analysis of electromagnetic scattering from arbitrarily shaped three-dimensional (3-D) homogeneous dielectric body in the frequency domain. The four integral equations treated here are the electric field integral equation (EFIE), the magnetic field integral equation (MFIE), the combined field integral equation (CFIE), and the PMCHW (Poggio, Miller, Chang, Harrington, and Wu) formulation. For the CFIE case, we propose eight separate formulations with different combinations of expansion and testing functions that result in sixteen different formulations of CFIE. One of the objectives of this paper is to illustrate that not all CFIE are valid methodologies in removing defects, which occur at a frequency corresponding to an internal resonance of the structure. Numerical results involving the equivalent electric and magnetic currents, far scattered fields, and radar cross section (RCS) are presented for three canonical dielectric scatterers, viz. a sphere, a cube, and a finite circular cylinder, to illustrate which formulation works and which does not.

1. INTRODUCTION

The analysis of electromagnetic scattering from arbitrarily shaped 3-D homogeneous dielectric body in the frequency domain has been of considerable interest in recent years. In the analysis of dielectric bodies at frequencies, which correspond to an internal resonance of the structure, often spurious solutions are obtained for the EFIE or MFIE. One possible way of obtaining a unique solution at an internal resonant frequency of the structure under analysis is to combine a weighted linear sum of the EFIE with MFIE and thereby eliminate the spurious solutions [1]. This combination results in the CFIE. Although an integral equation formulation has been used for 3-D dielectric bodies in the frequency domain, only a few researchers have applied it to the analysis of scattering by arbitrarily shaped 3-D objects with triangular patch modeling [2–6].

The integral equation used in [2] and [5] is the PMCHW formulation, in which Rao-Wilton-Glisson (RWG) functions described in [7] has been used both as the basis and testing functions, to approximate both the electric and the magnetic currents. For the EFIE formulation [3], the electric current is expanded using the RWG functions, but the magnetic current is expanded using another set of basis functions given by $\hat{n} \times$ RWG which are point-wise spatially orthogonal to the RWG set. Here $\hat{n}$ is the unit normal pointing outward from the surface. In addition RWG is also used as the testing functions. Rao and Wilton proposed the CFIE with EFIE and MFIE for the analysis of scattering by arbitrarily shaped 3-D dielectric bodies for the first time [4]. In their work, RWG functions is used to approximate the electric current, but the magnetic current is approximated by $\hat{n} \times$ RWG as in [3], and a line testing is used. In a recent paper [6], Sheng et al. proposed a CFIE formulation for this problem. In their work the RWG functions are used as basis functions to approximate both the electric and magnetic currents, and RWG and $\hat{n} \times$ RWG functions are used as testing functions. This yields a well-conditioned matrix. They also presented a set of four CFIE formulations by dropping one of the testing terms in $\langle \mathrm{RWG}, \mathrm{EFIE}\rangle + \langle \hat{n} \times \mathrm{RWG}, \mathrm{EFIE}\rangle + \langle \mathrm{RWG}, \mathrm{MFIE}\rangle + \langle \hat{n} \times \mathrm{RWG}, \mathrm{MFIE}\rangle$.

In this work, we investigate various integral formulations and propose several combination of CFIE with different choices of testing functions. The goal is to illustrate that not all CFIE formulations are stable. This paper is organized as follows. In the next section, we describe the integral equation formulations such as EFIE, MFIE, CFIE, and PMCHW. In Section 3, the triangular patch basis functions are described and the numerical implementation of EFIE, MFIE, CFIE, and PMCHW is developed in detail. Section 4 presents several formulations of CFIE and some numerical solutions. In Section 5, numerical results for a dielectric sphere, a cube, and a finite circular cylinder are presented and compared with other available solutions. Finally, conclusions are presented in Section 6.

2. INTEGRAL EQUATIONS

In this section, we describe the detailed mathematical steps to obtain a pair of coupled integral equations to analyze the electromagnetic scattering from arbitrary shaped 3-D homogeneous dielectric bodies. From these set of integral equations, we develop EFIE, MFIE, PMCHW, and CFIE. For the sake of clarity, we present the formulations for a single dielectric body. Extending the formulation to handle multiple dielectric bodies is quite straightforward.

Consider a homogeneous dielectric body with a permittivity ε_2 and a permeability μ_2 placed in an infinite homogeneous medium with a permittivity ε_1 and a permeability μ_1. A lossy material body can be handled by considering ε_2, or μ_2, to be complex. The structure is now illuminated by an incident plane wave denoted by $(\underline{E}^i, \underline{H}^i)$. It may be noted that the incident field is defined to be that which would exist in space if the structure were not present. By invoking the equivalence principle [8], the following two problems are formulated, which are valid for the regions external and internal to the dielectric body, in terms of the equivalent electric and magnetic current $\underline{J}$ and $\underline{M}$ on the surface S of dielectric body, respectively.

By enforcing the continuity of the tangential electric and magnetic field at S_-, where S_- is selected to be slightly interior to S, the following equations are obtained:

$$[-\underline{E}_1^s(\underline{J},\underline{M})]_{\tan} = [\underline{E}^i]_{\tan} \tag{1}$$

$$[-\underline{H}_1^s(\underline{J},\underline{M})]_{\tan} = [\underline{H}^i]_{\tan} \tag{2}$$

where the subscript '1' represents the medium in which the scattered field $(\underline{E}_1^s, \underline{H}_1^s)$ is computed. Because the field in the interior region to the dielectric body is zero, the entire space is now filled with the dielectric medium (ε_1, μ_1), which originally was only external to the dielectric body. By enforcing the continuity of the tangential electric and magnetic field at S_+, where S_+ is the surface slightly exterior to S, the following equations are derived:

$$[-\underline{E}_2^s(\underline{J},\underline{M})]_{\tan} = 0 \tag{3}$$

$$[-\underline{H}_2^s(\underline{J},\underline{M})]_{\tan} = 0 \tag{4}$$

where the subscript '2' represents the medium in which the scattered field $(\underline{E}_2^s, \underline{H}_2^s)$ is evaluated. Again since the fields in the external region to the material body is zero, the external region can be replaced by the material (ε_2, μ_2) so that now the currents are located in a homogeneous medium with properties of the material which was internal to the material body of the original problem. In (1)–(4), the subscript 'tan' refers to the tangential component only.

Now that both problems (internal and external) are formulated in terms of electric and magnetic currents radiating in a homogeneous medium the various fields can be expressed analytically. The scattered electric and magnetic fields due to the electric current $\underline{J}$ and magnetic current $\underline{M}$ are given by

$$\underline{E}_v^s(\underline{J}) = -j\omega\underline{A}_v - \nabla\phi_v \tag{5}$$

$$\underline{E}_v^s(\underline{M}) = -\frac{1}{\varepsilon_v}\nabla\times\underline{F}_v \tag{6}$$

$$\underline{H}_v^s(\underline{J}) = \frac{1}{\mu_v}\nabla\times\underline{A}_v \tag{7}$$

$$\underline{H}_v^s(\underline{M}) = -j\omega\underline{F}_v - \nabla\psi_v \tag{8}$$

where the magnetic and electric vector potentials $\underline{A}_v$ and $\underline{F}_v$, and the scalar potentials ϕ_v and ψ_v, for $v = 1, 2$ are given by

$$\underline{A}_v(\underline{r}) = \frac{\mu_v}{4\pi} \int_S \underline{J}(\underline{r}') G_v(\underline{r}, \underline{r}') dS' \tag{9}$$

$$\underline{F}_v(\underline{r}) = \frac{\varepsilon_v}{4\pi} \int_S \underline{M}(\underline{r}') G_v(\underline{r}, \underline{r}') dS' \tag{10}$$

$$\phi_v(\underline{r}) = \frac{j}{4\pi\omega\varepsilon_v} \int_S \nabla'_S \cdot \underline{J}(\underline{r}') G_v(\underline{r}, \underline{r}') dS' \tag{11}$$

$$\psi_v(\underline{r}) = \frac{j}{4\pi\omega\mu_v} \int_S \nabla'_S \cdot \underline{M}(\underline{r}') G_v(\underline{r}, \underline{r}') dS' \tag{12}$$

$$G_v(\underline{r}, \underline{r}') = \frac{e^{-jk_v R}}{R}; \qquad R = |\underline{r} - \underline{r}'|. \tag{13}$$

In (9)–(12), a $e^{j\omega t}$ time dependence has been assumed and suppressed. R represents the distance between the observation point $\underline{r}$ and the source point $\underline{r}'$ with respect to a global coordinate origin. $k_v = \omega\sqrt{\mu_v \varepsilon_v}$ is the wave number. ω is the angular frequency in rad/sec. Note that v is either 1 or 2 depending on the medium in which the currents $\underline{J}$ and $\underline{M}$ are radiating. Equation (13) represents the Green's function for a homogeneous medium.

In (1)–(4), there are two unknowns $\underline{J}$ and $\underline{M}$, and four equations relating them. It is possible to develop various combinations for the solution of these equations. If we take only two equations, (1) and (3), we have the EFIE formulation. Dual to the EFIE formulation, we can obtain the MFIE formulation by choosing only (2) and (4) from the set (1)–(4). However, both EFIE and MFIE formulations fail at frequencies at which the surface S, when covered by a perfect electric conductor and filled with the materials of the exterior medium, forms a resonant cavity. An alternative way of combining the four equations is the PMCHW formulation. In this formulation, the set of four equations is reduced to two by adding (1) to (3) and (2) to (4). This gives a pair of equations

$$[-\underline{E}_1^s(\underline{J}, \underline{M}) - \underline{E}_2^s(\underline{J}, \underline{M})]_{\tan} = [\underline{E}^i]_{\tan} \tag{14}$$

$$[-\underline{H}_1^s(\underline{J}, \underline{M}) - \underline{H}_2^s(\underline{J}, \underline{M})]_{\tan} = [\underline{H}^i]_{\tan} \tag{15}$$

For the CFIE formulation, a set of two integral equations are formed from the set (1)–(4) using the following form

$$[-\underline{E}_v^s(\underline{J}, \underline{M})]_{\tan} + \eta_1[-\underline{H}_v^s(\underline{J}, \underline{M})]_{\tan} = \begin{cases} [\underline{E}^i]_{\tan} + \eta_1[\underline{H}^i]_{\tan}, & v = 1 \\ 0, & v = 2 \end{cases} \tag{16}$$

where η_1 is the wave impedance of region 1.

3. NUMERICAL IMPLEMENTATION

The structure to be analyzed is approximated by planar triangular patches. The triangular patches have the ability to conform to any geometrical surface of boundary. As in reference [7], we define the vector basis function associated the n^{th} edge as

$$\underline{f}_n(\underline{r}) = \underline{f}_n^+(\underline{r}) + \underline{f}_n^-(\underline{r}) \tag{17a}$$

$$\underline{f}_n^\pm(\underline{r}) = \begin{cases} \dfrac{l_n}{2A_n^\pm}\underline{\rho}_n^\pm, & \underline{r} \in T_n^\pm \\ 0, & \underline{r} \notin T_n^\pm \end{cases} \tag{17b}$$

where l_n is the length of the n^{th} edge and $A_n^\pm$ is the area of the triangle $T_n^\pm$. $\underline{\rho}_n^\pm$ is the position vector with respect to the free vertex of $T_n^\pm$. Fig. 1 illustrates the various variables. The position vector $\underline{\rho}_n^+$ is directed from the free vertex of T_n^+ toward points in T_n^+. Similar remarks apply to the position $\underline{\rho}_n^-$ except that it is directed toward the free vertex of T_n^-. The surface divergence of (17) is given by

$$\nabla_S \cdot \underline{f}_n(\underline{r}) = \nabla_S \cdot \underline{f}_n^+(\underline{r}) + \nabla_S \cdot \underline{f}_n^-(\underline{r}) \tag{18a}$$

$$\nabla_S \cdot \underline{f}_n^\pm(\underline{r}) = \begin{cases} \pm\dfrac{l_n}{A_n^\pm}\underline{\rho}_n^\pm, & \underline{r} \in T_n^\pm \\ 0, & \underline{r} \notin T_n^\pm \end{cases} \tag{18b}$$

Another vector basis function is defined through [3]

$$\underline{g}_n(\underline{r}) = \hat{n} \times \underline{f}_n(\underline{r}). \tag{19}$$

The functions $\underline{f}_n$ and $\underline{g}_n$ are point-wise orthogonal in the triangle pair. These functions are used in the four formulations, EFIE, MFIE, PMCHW, and CFIE. The various expansion and testing functions for the various currents used in each formulation are summarized in Table 1.

We consider the numerical procedure in detail. Although the EFIE formulation is described in [3] and [4], we develop the implementation procedure in detail, from which other formulations are derived simply. The evaluation of integrals in the matrix elements is considered in the Appendix.

3.1. EFIE Formulation

The electric current $\underline{J}$ and the magnetic current $\underline{M}$ on the structure to be analyzed may be approximated in terms of two vector basis

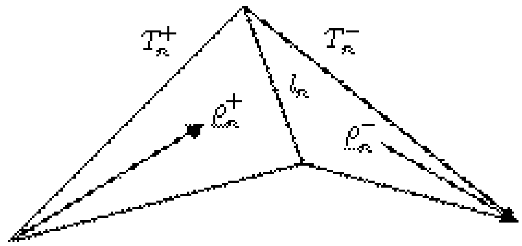

Figure 1. Two triangular patches associated with an edge.

Table 1. Expansion and testing functions used in four formulations.

Formulation	Testing function	Current expansion function	
		$\underline{J}$	$\underline{M}$
EFIE	$\underline{f}_m$	$\underline{f}_n$	$\hat{n} \times \underline{f}_n$
MFIE	$\underline{f}_m$	$\hat{n} \times \underline{f}_n$	$\underline{f}_n$
PMCHW	$\underline{f}_m$	$\underline{f}_n$	$\underline{f}_n$
CFIE	$\underline{f}_m + \hat{n} \times \underline{f}_m$	$\underline{f}_n$	$\underline{f}_n$

functions (17) and (19) as

$$\underline{J}(\underline{r}) = \sum_{n=1}^{N} I_n \underline{f}_n(\underline{r}) \tag{20}$$

$$\underline{M}(\underline{r}) = \sum_{n=1}^{N} M_n \underline{g}_n(\underline{r}) \tag{21}$$

where I_n and M_n are constants yet to be determined and N is the number of edges on the dielectric surface for the triangulated model approximating the surface of the dielectric body. The next step in the application of the method of moments is to select a suitable testing procedure. As testing functions, we choose the expansion functions in (17). Since all the functions are real, we can use the symmetric product

$$\langle \underline{f} \cdot \underline{g} \rangle = \int_S \underline{f} \cdot \underline{g} dS. \tag{22}$$

We test (1) and (3) with $\underline{f}_m$, yielding

$$\langle \underline{f}_m, -\underline{E}_v^s(\underline{J})\rangle + \langle \underline{f}_m, -\underline{E}_v^s(\underline{M})\rangle = \begin{cases} \langle \underline{f}_m, \underline{E}^i\rangle, & v = 1 \\ 0, & v = 2 \end{cases} \tag{23}$$

for $m = 1, 2, \ldots, N$. The first term in (23) with (5) is given by

$$\langle \underline{f}_m, -\underline{E}_v^s(\underline{J})\rangle = \langle \underline{f}_m, j\omega \underline{A}_v\rangle + \langle \underline{f}_m, \nabla\phi_v\rangle. \tag{24}$$

Substituting (9) into the testing of the magnetic vector potential and using the current expansion (20), we have

$$\langle \underline{f}_m, j\omega \underline{A}_v\rangle = \sum_{n=1}^{N} j\omega\mu_v A_{mn,v} I_n \tag{25}$$

where

$$A_{mn,v} = \frac{1}{4\pi}\int_S \underline{f}_m(\underline{r}) \cdot \int_S \underline{f}_n(\underline{r}') G_v(\underline{r}, \underline{r}') dS' dS. \tag{26}$$

Next, we consider the testing of the gradient of the electric scalar potential in (24). Using the vector identity $\nabla \cdot \phi\underline{A} = \underline{A} \cdot \nabla\phi + \phi\nabla \cdot \underline{A}$ and the properties of the basis function [9], we have

$$\langle \underline{f}_m, \nabla\phi_v\rangle = -\int_S \nabla_S \cdot \underline{f}_m \phi_v dS. \tag{27}$$

Substitution of (11) into (27) with current expansion (20) yields

$$\langle \underline{f}_m, \nabla\phi_v\rangle = \sum_{n=1}^{N} \left(-\frac{j}{\omega\varepsilon}\right) B_{mn,v} I_n \tag{28}$$

where

$$B_{mn,v} = \frac{1}{4\pi}\int_S \nabla_S \cdot \underline{f}_m(\underline{r}) \int_S \nabla_S' \cdot \underline{f}_n(\underline{r}') G_v(\underline{r}, \underline{r}') dS' dS. \tag{29}$$

Therefore, substitution of (25) and (28) into (24) yields

$$\langle \underline{f}_m, -\underline{E}_v^s(\underline{J})\rangle = \sum_{n=1}^{N} jk_v\eta_v \left(A_{mn,v} - \frac{B_{mn,v}}{k_v^2}\right) I_n \tag{30}$$

where $k_v\eta_v = \omega\mu_v$ and η_v is the intrinsic impedance of the medium numbered v.

Now, consider the second term of (23). Extracting the Cauchy principal value from the curl term on the planar surface in (6) with (10), we may write

$$\frac{1}{\varepsilon_v}\nabla\times\underline{F}_v(\underline{r}) = \pm\frac{1}{2}\hat{n}\times\underline{M}(\underline{r}) + \frac{1}{\varepsilon_v}\nabla\times\underline{\tilde{F}}_v(\underline{r}) \tag{31}$$

where $\underline{\tilde{F}}_v$ is defined by (10) with $\underline{r} = \underline{r}'$, or $R = 0$, term removed from the integration. In (31), the positive sign is used when $v = 1$ and negative sign otherwise. Using (31), we can get

$$\langle\underline{f}_m, -\underline{E}_v^s(\underline{M})\rangle = \langle\underline{f}_m, \pm\frac{1}{2}\hat{n}\times\underline{M}\rangle + \langle\underline{f}_m, \frac{1}{\varepsilon_v}\nabla\times\underline{\tilde{F}}_v\rangle. \tag{32}$$

Consider the inner product integrals in (32). Substitution of the magnetic current expansion defined in (21) in the first term located in the right-hand side of (32) yields

$$\langle\underline{f}_m, \pm\frac{1}{2}\hat{n}\times\underline{M}\rangle = \sum_{n=1}^{N} C_{mn,v}M_n \tag{33}$$

where

$$C_{mn,v} = \begin{cases} +C_{mn}, & v = 1 \\ -C_{mn}, & v = 2 \end{cases} \tag{34}$$

$$C_{mn} = \frac{1}{2}\int_S \underline{f}_m(\underline{r})\cdot\hat{n}\times\underline{g}_n(\underline{r})dS. \tag{35}$$

Next, we consider the second term on the right-hand side of (32). Using (10) in association with (21), we obtain

$$\langle\underline{f}_m, \frac{1}{\varepsilon_v}\nabla\times\underline{\tilde{F}}_v\rangle = \sum_{n=1}^{N} D_{mn,v}M_n \tag{36}$$

where

$$D_{mn,v} = \frac{1}{4\pi}\int_S \underline{f}_m(\underline{r})\cdot\int_S \underline{g}_n(\underline{r}')\nabla' G_v(\underline{r},\underline{r}')dS'dS. \tag{37}$$

Substitution of (33) and (36) into (32) yields

$$\langle\underline{f}_m, -\underline{E}_v^s(\underline{M})\rangle = \sum_{n=1}^{N}(C_{mn,v} + D_{mn,v})M_n. \tag{38}$$

Finally, substituting (30) and (38) into (23), we obtain

$$\sum_{n=1}^{N} jk_v\eta_v\left(A_{mn,v}-\frac{B_{mn,v}}{k_v^2}\right)I_n+\sum_{n=1}^{N}(C_{mn,v}+D_{mn,v})M_n=V_{m,v}^E. \quad (39)$$

where

$$V_{m,v}^E=\begin{cases}\int_S \underline{f}_m(\underline{r})\cdot\underline{E}^i(\underline{r})dS, & v=1\\ 0, & v=2\end{cases}. \quad (40)$$

Equation (39) is associated with each edge, $m=1,2,\ldots,N$. Therefore (39) may be written in a matrix form as

$$\begin{bmatrix}[jk_1\eta_1(A_{mn,1}-B_{mn,1}/k_1^2)] & [C_{mn,1}+D_{mn,1}]\\ [jk_2\eta_2(A_{mn,2}-B_{mn,2}/k_2^2)] & [C_{mn,2}+D_{mn,2}]\end{bmatrix}\begin{bmatrix}[I_n]\\ [M_n]\end{bmatrix}=\begin{bmatrix}[V_{m,1}^E]\\ [V_{m,2}^E]\end{bmatrix}. \quad (41)$$

Equation (41) is a $2N\times 2N$ system of linear equations.

3.2. MFIE Formulation

In this paper, MFIE has been defined in a different form from that of [4]. It is the dual of EFIE. For the MFIE formulation, the electric current $\underline{J}$ and the magnetic current $\underline{M}$ may be approximated by

$$\underline{J}(\underline{r}) = \sum_{n=1}^{N} I_n\underline{g}_n(\underline{r}) \quad (42)$$

$$\underline{M}(\underline{r}) = \sum_{n=1}^{N} M_n\underline{f}_n(\underline{r}). \quad (43)$$

These current expansions are similar to (20) and (21) in the EFIE formulation. Using (22), we test (2) and (4) with $\underline{f}_m$, yielding

$$\langle\underline{f}_m,-\underline{H}_v^s(\underline{J})\rangle+\langle\underline{f}_m,-\underline{H}_v^s(\underline{M})\rangle=\begin{cases}\langle\underline{f}_m,\underline{H}^i\rangle, & v=1\\ 0, & v=2\end{cases}. \quad (44)$$

Using a formulation as described for the EFIE formulation, we get

$$-\sum_{n=1}^{N}(C_{mn,v}+D_{mn,v})I_n+\sum_{n=1}^{N} j\frac{k_v}{\eta_v}\left(A_{mn,v}-\frac{B_{mn,v}}{k_v^2}\right)M_n=V_{mn,v}^H \quad (45)$$

where

$$V_{m,v}^H = \begin{cases} \int_S \underline{f}_m(\underline{r}) \cdot \underline{H}^i(\underline{r}) dS, & v = 1 \\ 0, & v = 2 \end{cases}. \tag{46}$$

We note that (45) can be obtained directly from (39) by using the principle of duality [8]. Equation (45) is associated with each edge, $m = 1, 2, \ldots, N$. Therefore, (45) may be written in a matrix form as

$$\begin{bmatrix} [-(C_{mn,1}+D_{mn,1})] & [jk_1/\eta_1(A_{mn,1}-B_{mn,1}/k_1^2)] \\ [-(C_{mn,2}+D_{mn,2})] & [jk_2/\eta_2(A_{mn,2}-B_{mn,2}/k_2^2)] \end{bmatrix} \begin{bmatrix} [I_n] \\ [M_n] \end{bmatrix} = \begin{bmatrix} [V_{m,1}^H] \\ [V_{m,2}^H] \end{bmatrix}. \tag{47}$$

Equation (47) is dual to (41) and the integrals $A_{mn,v}$, $B_{mn,v}$, $C_{mn,v}$, and $D_{mn,v}$ in the matrix elements are same as those of (41).

3.3. PMCHW Formulation

In the PMCHW integral equations (14) and (15), the electric current $\underline{J}$ and the magnetic current $\underline{M}$ may be approximated by (20) and (43), respectively. Also, $\underline{f}_m$ is used as the testing function. Applying the testing procedure to (14), we get

$$\langle \underline{f}_m, -\underline{E}_1^s(\underline{J}, \underline{M}) - \underline{E}_2^s(\underline{J}, \underline{M}) \rangle = \langle \underline{f}_m, \underline{E}^i \rangle. \tag{48}$$

Equation (48) is evaluated simply by using (39), which is derived from (23). The result is given by

$$\sum_{n=1}^{N} \sum_{v=1}^{2} jk_v \eta_v \left(A_{mn,v} - \frac{B_{mn,v}}{k_v^2} \right) I_n + \sum_{n=1}^{N} \sum_{v=1}^{2} D_{mn,v} M_n = V_m^E \tag{49}$$

where

$$V_m^E = \int_S \underline{f}_m(\underline{r}) \cdot \underline{E}^i(\underline{r}) dS. \tag{50}$$

In (49), $A_{mn,v}$ and $B_{mn,v}$ are same as (26) and (29), respectively. Because the expansion functions of the magnetic current are different, $D_{mn,v}$ is given by

$$D_{mn,v} = \frac{1}{4\pi} \int_S \underline{f}_m(\underline{r}) \cdot \int_S \underline{f}_n(\underline{r}') \nabla' G_v(\underline{r}, \underline{r}') dS' dS. \tag{51}$$

Note that the first term located in the right-hand side of (31) is eliminated by adding $\underline{E}_1^s$ to $\underline{E}_2^s$ in (48). Therefore, the term $C_{mn,v}$ is not seen in (49).

Next, we apply the testing procedure to (15), we get

$$\langle \underline{f}_m, -\underline{H}_1^s(\underline{J}, \underline{M}) - \underline{H}_2^s(\underline{J}, \underline{M})\rangle = \langle \underline{f}_m, \underline{H}^i\rangle. \tag{52}$$

Similarly, by using the result of the MFIE formulation given by (45), (52) can be expressed as

$$-\sum_{n=1}^{N}\sum_{v=1}^{2} D_{mn,v} I_n + \sum_{n=1}^{N}\sum_{v=1}^{2} j\frac{k_v}{\eta_v}\left(A_{mn,v} - \frac{B_{mn,v}}{k_v^2}\right) M_n = V_m^H \tag{53}$$

where

$$V_m^H = \int_S \underline{f}_m(\underline{r}) \cdot \underline{H}^i(\underline{r}) dS. \tag{54}$$

The integral of elements $A_{mn,v}$, $B_{mn,v}$, and $D_{mn,v}$ are same as those in (49), respectively. We note that (53) can be obtained directly from (49) by using duality without additional any effort. Equation (49) and (53) are associated with each edge, $m = 1, 2, \ldots, N$. Therefore, we have a matrix equation defined by

$$\begin{bmatrix} \left[\sum_{v=1}^{2} jk_v\eta_v(A_{mn,v} - B_{mn,v}/k_v^2)\right] & \left[\sum_{v=1}^{2} D_{mn,v}\right] \\ \left[-\sum_{v=1}^{2} D_{mn,v}\right] & \left[\sum_{v=1}^{2} jk_v/\eta_v(A_{mn,2} - B_{mn,v}/k_v^2)\right] \end{bmatrix} \cdot \begin{bmatrix} [I_n] \\ [M_n] \end{bmatrix} = \begin{bmatrix} [V_m^E] \\ [V_m^H] \end{bmatrix}. \tag{55}$$

3.4. CFIE Formulation

In the CFIE formulation, the basis functions defined in (17) are used to expand both the electric current $\underline{J}$ and the magnetic current $\underline{M}$ as in the PMCHW formulation and then we use $\underline{f}_m + \underline{g}_m$ as the testing functions to convert the CFIE into a matrix equation. Applying the testing procedure to (16), we get

$$\begin{aligned} &\langle \underline{f}_m + \underline{g}_m, -\underline{E}_v^s\rangle + \eta_1\langle \underline{f}_m + \underline{g}_m, -\underline{H}_v^s\rangle \\ &\quad = \begin{cases} \langle \underline{f}_m + \underline{g}_m, \underline{E}^i\rangle + \eta_1\langle \underline{f}_m + \underline{g}_m, \underline{H}^i\rangle, & v = 1 \\ 0, & v = 2 \end{cases}. \end{aligned} \tag{56}$$

Another way to represent the set of four boundary integral equations in (1)–(4) is the following [1]:

$$-\hat{n} \times \underline{E}_1^s(\underline{J}, \underline{M}) = \hat{n} \times \underline{E}^i \tag{57}$$

$$-\hat{n} \times \underline{H}_1^s(\underline{J}, \underline{M}) = \hat{n} \times \underline{H}^i \tag{58}$$

$$-\hat{n} \times \underline{E}_2^s(\underline{J}, \underline{M}) = 0 \tag{59}$$

$$-\hat{n} \times \underline{H}_2^s(\underline{J}, \underline{M}) = 0. \tag{60}$$

Adding the set of equations (1)–(4) to the set of equations (57)–(60), respectively, we may obtain another CFIE similar to (16). By applying the testing procedure with $\underline{f}_m$ as testing functions, we get

$$\begin{aligned} &\langle \underline{f}_m, -\underline{E}_v^s - \hat{n} \times \underline{E}_v^s \rangle + \eta_1 \langle \underline{f}_m, -\underline{H}_v^s - \hat{n} \times \underline{H}_v^s \rangle \\ &\quad = \begin{cases} \langle \underline{f}_m, \underline{E}^i + \hat{n} \times \underline{E}^i \rangle + \eta_1 \langle \underline{f}_m, \underline{H}^i + \hat{n} \times \underline{H}^i \rangle, & v = 1 \\ 0, & v = 2 \end{cases} \end{aligned} \tag{61}$$

By using the vector identity $\underline{A} \cdot \underline{B} \times \underline{C} = \underline{C} \cdot \underline{A} \times \underline{B}$, we obtain the following relationship

$$\langle \underline{f}_m, \hat{n} \times \underline{E} \rangle = \langle -\hat{n} \times \underline{f}_m, \underline{E} \rangle = \langle -\underline{g}_m, \underline{E} \rangle \tag{62}$$

where $\underline{E}$ denotes the electric or the magnetic field. Using (62), we may write (61) as

$$\begin{aligned} &\langle \underline{f}_m - \underline{g}_m, -\underline{E}_v^s \rangle + \eta_1 \langle \underline{f}_m - \underline{g}_m, -\underline{H}_v^s \rangle \\ &\quad = \begin{cases} \langle \underline{f}_m - \underline{g}_m, \underline{E}^i \rangle + \eta_1 \langle \underline{f}_m - \underline{g}_m, \underline{H}^i \rangle, & v = 1 \\ 0, & v = 2 \end{cases}. \end{aligned} \tag{63}$$

It is important to note that the testing function is $\underline{f}_m + \underline{g}_m$ in (56) and $\underline{f}_m - \underline{g}_m$ in (63) for the same CFIE. We also note that we can formulate by testing either EFIE or MFIE with $\underline{f}_m + \underline{g}_m$ or $\underline{f}_m - \underline{g}_m$. This different ways to obtain the CFIE formulation results in eight different formulations by combining $\langle \underline{f}_m \pm \underline{g}_m, \underline{E} \rangle \pm \langle \underline{f}_m \pm \underline{g}_m, \underline{H} \rangle$. For this, we present a general expression for CFIE using the four parameters in conjunction with the testing functions as

$$\begin{aligned} &(1-\kappa)\langle f_E \underline{f}_m + g_E \underline{g}_m, -\underline{E}_v^s \rangle + \kappa\eta_1 \langle f_H \underline{f}_m + g_H \underline{g}_m, -\underline{H}_v^s \rangle \\ &= \begin{cases} (1-\kappa)\langle f_E \underline{f}_m + g_E \underline{g}_m, \underline{E}^i \rangle + \kappa\eta_1 \langle f_H \underline{f}_m + g_H \underline{g}_m, \underline{H}^i \rangle, & v=1 \\ 0, & v=2 \end{cases} \end{aligned} \tag{64}$$

where κ is the usual combination parameter which can have any value between 0 and 1. The testing coefficients f_E, g_E, f_H, and g_H may be $+1$ or -1. If $f_E = 1$, $g_E = 1$, $f_H = 1$, and $g_H = 1$, (64) is the same as (56). Equation (64) becomes (63) when $f_E = 1$, $g_E = -1$, $f_H = 1$, and $g_H = -1$.

To convert (64) into a matrix equation by using the above parameters to result in EFIE, MFIE, and CFIE formulations, we separate (64) into two categories, the electric field and the magnetic field parts. First, we write the equation related to the electric field only from (64) as

$$\langle f_E\underline{f}_m + g_E\underline{g}_m, -\underline{E}_v^s(\underline{J}, \underline{M})\rangle = \begin{cases} \langle f_E\underline{f}_m + g_E\underline{g}_m, \underline{E}^i\rangle, & v = 1 \\ 0, & v = 2 \end{cases}. \quad (65)$$

This equation is termed as the TENE formulation in [6]. Equation (65) is of the same form as (23) except the testing functions are different. Thus, by using a similar procedure as in EFIE, we have

$$\sum_{n=1}^{N} jk_v\eta_v \left(A_{mn,v}^E - \frac{B_{mn,v}^E}{k_v^2}\right) I_n + \sum_{n=1}^{N}(C_{mn,v}^E + D_{mn,v}^E)M_n = V_{m,v}^E \quad (66)$$

where

$$A_{mn,v}^E = f_E A_{mn,v}^f + g_E A_{mn,v}^g \quad (67)$$

$$B_{mn,v}^E = f_E B_{mn,v}^f + g_E B_{mn,v}^g \quad (68)$$

$$C_{mn,v}^E = \begin{cases} +C_{mn}^E, & v = 1 \\ -C_{mn}^E, & v = 2 \end{cases} \quad (69)$$

$$C_{mn}^E = f_E C_{mn}^f + g_E C_{mn}^g \quad (70)$$

$$D_{mn,v}^E = f_E D_{mn,v}^f + g_E D_{mn,v}^g \quad (71)$$

$$V_{m,v}^E = \begin{cases} \int_S (f_E\underline{f}_m + g_E\underline{g}_m)\cdot\underline{E}^i dS, & v = 1 \\ 0, & v = 2 \end{cases}. \quad (72)$$

In (67)–(71), the elements having the superscript 'f' are the inner products with $\underline{f}_m$ and the elements having superscript 'g' are the inner products with $\underline{g}_m$. These elements are given by

$$A_{mn,v}^f = \frac{1}{4\pi}\int_S \underline{f}_m(\underline{r})\cdot\int_S \underline{f}_n(\underline{r}')G_v(\underline{r}, \underline{r}')dS'dS \quad (73)$$

$$A^g_{mn,v} = \frac{1}{4\pi}\int_S \underline{g}_m(\underline{r})\cdot\int_S \underline{f}_n(\underline{r}')G_v(\underline{r},\underline{r}')dS'dS \tag{74}$$

$$B^f_{mn,v} = \frac{1}{4\pi}\int_S \nabla_S\cdot\underline{f}_m(\underline{r})\int_S \nabla'_S\cdot\underline{f}_n(\underline{r}')G_v(\underline{r},\underline{r}')dS'dS \tag{75}$$

$$B^g_{mn,v} = \frac{1}{4\pi}\int_S \underline{g}_m(\underline{r})\cdot\int_S \nabla'_S\cdot\underline{f}_n(\underline{r}')\nabla' G_v(\underline{r},\underline{r}')dS'dS \tag{76}$$

$$C^f_{mn} = \frac{1}{2}\int_S \underline{f}_m(\underline{r})\cdot\hat{n}\times\underline{f}_n(\underline{r})dS \tag{77}$$

$$C^g_{mn} = \frac{1}{2}\int_S \underline{g}_m(\underline{r})\cdot\hat{n}\times\underline{f}_n(\underline{r})dS \tag{78}$$

$$D^f_{mn,v} = \frac{1}{4\pi}\int_S \underline{f}_m\cdot\int_S \underline{f}_n\nabla' G_v(\underline{r},\underline{r}')dS'dS \tag{79}$$

$$D^g_{mn,v} = \frac{1}{4\pi}\int_S \underline{g}_m\cdot\int_S \underline{f}_n\nabla' G_v(\underline{r},\underline{r}')dS'dS \tag{80}$$

Therefore, we can obtain a matrix equation for (66) as

$$\begin{bmatrix} [jk_1\eta_1(A^E_{mn,1}-B^E_{mn,1}/k_1^2)] & [C^E_{mn,1}+D^E_{mn,1}] \\ [jk_2\eta_2(A^E_{mn,2}-B^E_{mn,2}/k_2^2)] & [C^E_{mn,2}+D^E_{mn,2}] \end{bmatrix}\begin{bmatrix}[I_n]\\ [M_n]\end{bmatrix} = \begin{bmatrix}[V^E_{m,1}]\\ [V^E_{m,2}]\end{bmatrix}. \tag{81}$$

Next, we write the equation corresponding to the magnetic field only from (64) as

$$\langle f_H\underline{f}_m + g_H\underline{g}_m, -\underline{H}^s_v(\underline{J},\underline{M})\rangle = \begin{cases} \langle f_H\underline{f}_m + g_H\underline{g}_m, \underline{H}^i\rangle, & v=1 \\ 0, & v=2 \end{cases} \tag{82}$$

This equation is termed as the THNH formulation in [6]. Equation (82) is of the same form as (44) except for the testing functions. Thus, by using a similar procedure as in the MFIE, we have

$$-\sum_{n=1}^{N}(C^H_{mn,v}+D^H_{mn,v})I_n + \sum_{n=1}^{N} j\frac{k_v}{\eta_v}\left(A^H_{mn,v} - \frac{B^H_{mn,v}}{k_v^2}\right)M_n = V^H_{m,v} \tag{83}$$

where

$$A^H_{mn,v} = f_H A^f_{mn,v} + g_H A^g_{mn,v} \tag{84}$$

$$B^H_{mn,v} = f_H B^f_{mn,v} + g_H B^g_{mn,v} \tag{85}$$

$$C^H_{mn,v} = \begin{cases} +C^H_{mn}, & v=1 \\ -C^H_{mn}, & v=2 \end{cases} \tag{86}$$

$$C^H_{mn} = f_H C^f_{mn} + g_H C^g_{mn} \tag{87}$$

$$D^H_{mn,v} = f_H D^f_{mn,v} + g_H D^g_{mn,v} \tag{88}$$

$$V^H_{m,v} = \begin{cases} \int_S (f_H \underline{f}_m + g_H \underline{g}_m) \cdot \underline{H}^i dS, & v = 1 \\ 0, & v = 2 \end{cases}. \tag{89}$$

In (84)–(88), the elements with superscript superscript 'f' and 'g' are same as those in (73)–(80), respectively. Note that we may obtain (83) directly from (66) by using duality. The matrix equation corresponding to (83) is given by

$$\begin{bmatrix} [-(C^H_{mn,1}+D^H_{mn,1})] & [jk_1/\eta_1(A^H_{mn,1}-B^H_{mn,1}/k_1^2)] \\ [-(C^H_{mn,2}+D^H_{mn,2})] & [jk_2/\eta_2(A^H_{mn,2}-B^H_{mn,2}/k_2^2)] \end{bmatrix} \begin{bmatrix} [I_n] \\ [M_n] \end{bmatrix} = \begin{bmatrix} [V^H_{m,1}] \\ [V^H_{m,2}] \end{bmatrix}. \tag{90}$$

We may rewrite the matrix equations (81) and (90), respectively, as

$$[Z^E_{mn}][C_n] = [V^E_m] \tag{91}$$

$$[Z^H_{mn}][C_n] = [V^H_m] \tag{92}$$

where $C_n = I_n$ and $C_{(N+n)} = M_n$ for $n = 1, 2, \ldots, N$. Finally, by combining TENE and THNH given in (91) and (92), respectively, we have a matrix equation associated with (64) as

$$[Z_{mn}][C_n] = [V_m] \tag{93}$$

where the matrix elements are given by

$$Z_{mn} = (1-\kappa) Z^E_{mn} + \kappa \eta_1 Z^H_{mn} \tag{94}$$

$$V_m = (1-\kappa) V^E_m + \kappa \eta_1 V^H_m \tag{95}$$

for $m = 1, 2, \ldots, 2N$ and $n = 1, 2, \ldots, 2N$.

4. STUDY OF THE VARIOUS FORMULATIONS

In this section, we study the general CFIE formulation described by (64), which results in the matrix equation (93). As discussed in the above section, we have eight different formulations for a CFIE formulation with different testing coefficients. They are summarized along with the appropriate testing coefficients in Table 2. To obtain numerical results, we consider a dielectric sphere having a diameter of 1 m and a relative permittivity $\varepsilon_r = 2$, centered at the origin, as

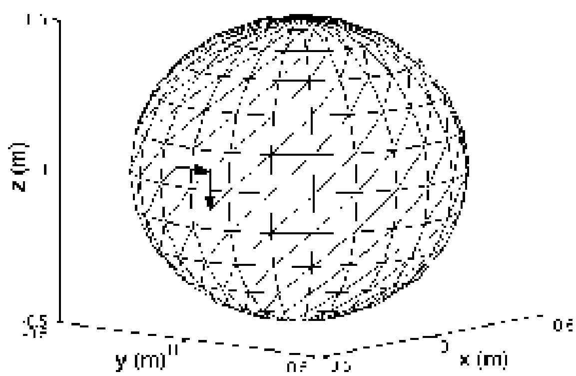

Figure 2. Triangle surface patching of a dielectric sphere (radius 0.5 m). θ- and ϕ-directed arrows represent position and direction of sampled currents $\underline{J}$ and $\underline{M}$, respectively.

Table 2. Eight CFIE formulations with the different combination of testing coefficients and the averaged difference of monostatic RCS between Mie and CFIE solution for the dielectric sphere in Fig. 2.

Formulation	Testing coefficients				$\Delta\sigma$ (dBm^2)
	f_E	g_E	f_H	g_H	
CFIE-1	1	1	1	1	1.02
CFIE-2	1	1	1	−1	4.61
CFIE-3	1	1	−1	1	0.40
CFIE-4	1	1	−1	−1	0.73
CFIE-5	1	−1	1	1	0.41
CFIE-6	1	−1	1	−1	0.85
CFIE-7	1	−1	−1	1	1.10
CFIE-8	1	−1	−1	−1	4.61

shown in Fig. 2. There are twelve and twenty-four divisions along θ and ϕ directions, respectively. This results in a sphere discretized by 528 patches and 792 edges. In the numerical calculation, the sphere is illuminated from the top by an incident x-polarized plane wave with the propagation vector $\hat{k} = -\hat{z}$. The analysis is to be done over a frequency range of $0 < f \leq 400\,\text{MHz}$ at an interval of $4\,\text{MHz}$ with 100 samples. Numerical results are compared with the Mie series solution

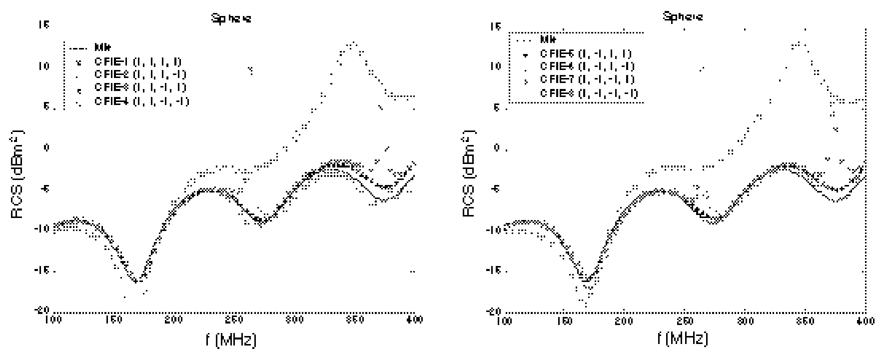

(a) (b)

Figure 3. Monostatic RCS of the dielectric sphere in Fig. 2 computed by eight CFIE formulations in Table 2.

between 100–400 MHz.

Fig. 3 represents the monostatic RCS of the sphere obtained for all the eight CFIE formulations described in Table 2. We used $\kappa = 0.5$. As evident from the figures, only two CFIE formulations, i.e., CFIE-3 and CFIE-5, compare well with the Mie solution. Other solutions break down as the interior resonance problem manifests itself or they just disagree with the Mie solution. It is interesting to note that CFIE-1 and CFIE-4 in Fig. 3(a) and CFIE-6 and CFIE-7 in Fig. 3(b) show a good agreement with the exact solution except near resonant frequencies of 262 and 369 MHz. Table 2 also shows the averaged difference between numerical and Mie solution for the monostatic RCS of the sphere. The averaged difference of monostatic RCS is computed by using the definition

$$\Delta\sigma = \frac{\sum^{M} |\sigma_{\text{Mie}} - \sigma_{\text{nume}}|}{M} \tag{96}$$

where σ denotes the RCS and M is the number of samples, which is 100 in this case.

There are four terms when one combines the TENE and THNH to form a CFIE, i.e., CFIE $=$ EFIE $+\, \hat{n} \times$ EFIE $+$ MFIE $+\, \hat{n} \times$ MFIE with $\underline{f}_m$ as the testing functions or CFIE $=$ EFIE $+$ MFIE with $\underline{f}_m + \underline{g}_m$ as the testing functions. It was suggested to drop one of these terms [6]. These formulations are named as TENE-TH, TENE-NH, TE-THNH, and NE-THNH, depending on which term is neglected. Applying this

Table 3. CFIE formulations with the different combination of testing coefficients and the averaged difference of normalized far field and monostatic RCS between Mie and CFIE solution for the dielectric sphere in Fig. 2.

Formulation		Testing coefficients				Δe_θ	Δe_ϕ	$\Delta\sigma$
		f_E	g_E	f_H	g_H	(mV)	(mV)	(dBm^2)
TENE-TH	(1)	1	1	1	0	12.0	16.7	0.79
	(2)	1	1	−1	0	4.1	6.4	0.30
	(3)	1	−1	1	0	4.7	6.0	0.34
	(4)	1	−1	−1	0	4.5	24.0	0.51
TENE-NH	(1)	1	1	0	1	3.5	12.9	0.28
	(2)	1	1	0	−1	7.8	32.1	0.22
	(3)	1	−1	0	1	2.4	20.3	0.37
	(4)	1	−1	0	−1	8.2	21.4	0.48
TE-THNH	(1)	1	0	1	1	9.4	5.5	0.61
	(2)	1	0	1	−1	8.1	9.8	0.59
	(3)	1	0	−1	1	8.7	7.2	0.55
	(4)	1	0	−1	−1	6.9	16.4	0.49
NE-THNH	(1)	0	1	1	1	5.1	12.9	0.42
	(2)	0	1	1	−1	5.7	16.4	0.48
	(3)	0	1	−1	1	5.7	21.5	0.52
	(4)	0	1	−1	−1	5.3	15.6	0.45

scheme to the eight different CFIE formulations of Table 2, we may have sixteen possible cases of CFIE with different testing coefficients, which are summarized in Table 3. The four figures in Fig. 4 show the monostatic RCS of the sphere displayed in Fig. 2. For comparison, we also present the Mie solution, which is represented by the solid curve, and all the results compare well. We note that the resonance problem is not observed in any one of the sixteen CFIE results. It should be noted that only two formulations of the CFIE in Table 2, for which any of the testing coefficient is not zero, give valid solutions, but in all the sixteen formulations one of the terms may be dropped as Table 3 without breaking down. There is a small difference between the exact solution in the high frequency region. We also present the averaged difference in the far field and in the monostatic RCS between

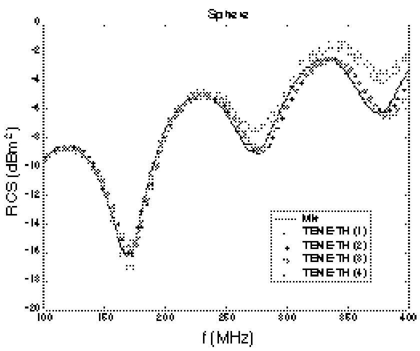

(a) TENE-TH

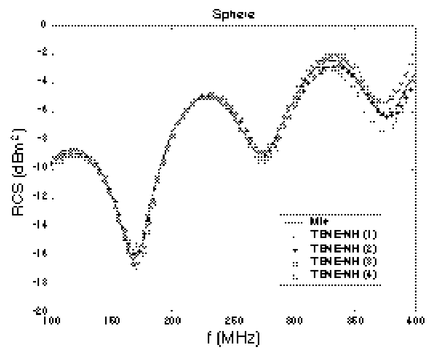

(b) TENE-NH

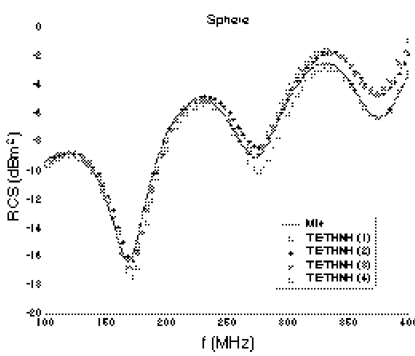

(c) TE-THNH

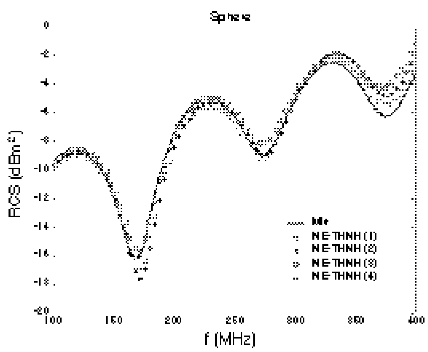

(d) NE-THNH

Figure 4. Monostatic RCS of the dielectric sphere in Fig. 2 computed by the sixteen CFIE formulations of Table 3.

the numerical and the Mie solution, which are summarized in Table 3. The averaged difference between the far field is also computed using the definition in (96). The smallest averaged difference in the RCS is $0.22\,\mathrm{dBm}^2$ for the TENE-NH (2) case. Comparing the differences in the far field, the results of TENE-TH (2) are most accurate for both θ- and ϕ-component in the far field. Fig. 5 compares the far field for TENE-TH (2) and TENE-NH (2) with the Mie solution. It is clearly seen that the far field of TENE-TH (2) give more accurate results than the TENE-NH (2) in this case. Numerical results using CFIE in the next section are presented using the testing coefficients as

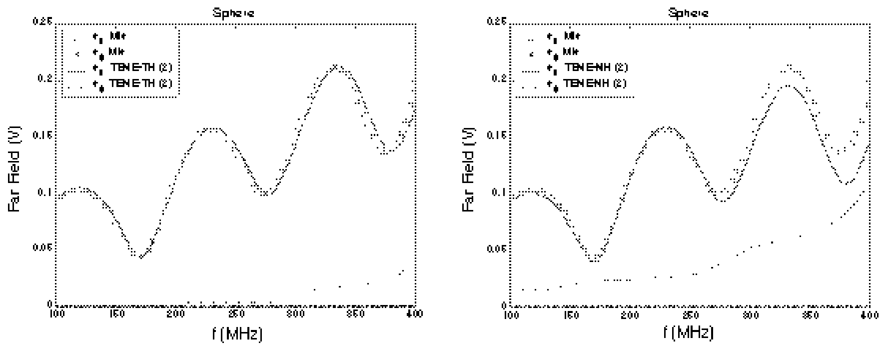

Figure 5. Comparison of the normalized far field for the dielectric sphere in Fig. 2 computed by Mie and CFIE solution. (a) TENE-TH (2) ($f_E = 1,\ g_E = 1,\ f_H = -1,\ g_H = 0$). (b) TENE-NH (2) ($f_E = 1,\ g_E = 1,\ f_H = 0,\ g_H = -1$).

$f_E = 1,\ g_E = 1,\ f_H = -1$, and $g_H = 1$ for TENE-THNH, which is CFIE-3 in Table 2 and includes TENE-TH (2).

Now, we investigate the effect of the combination parameter κ in (64). Fig. 6 compares the solutions of TENE-TH (2) with the Mie solution as we vary κ from 0.3 to 0.7 at an interval of 0.1. All the results agree well with the exact solution. Table 4 summarizes the averaged difference in the far field and monostatic RCS. It is evident from Fig. 6 and Table 4 that the solution of CFIE is not so sensitive to κ. The choice of κ can be selected within a wide range. For the results of the next section we choose $\kappa = 0.5$, which is not very critical.

5. NUMERICAL EXAMPLES

In this section, we present and compare the numerical results obtained from ten different formulations. These are EFIE, MFIE, PMCHW, and seven CFIE formulations that are described in Table 5. In this work, even though TENE or THNH consists of only electric or magnetic field, respectively, we consider this as a special case of CFIE with $\kappa = 0$ or $\kappa = 1$ to differentiate from EFIE or MFIE described in Section 3. The numerical results are obtained for representative 3-D scatterers with a relative permittivity $\varepsilon_r = 2$, viz. a sphere, a cube, and a cylinder. In the numerical calculation, the scatterers are illuminated from the top by an incident x-polarized plane wave with a propagation vector $\hat{k} = -\hat{z}$ as used in the above section. The frequency range over which

Table 4. Averaged difference of the normalized far field and monostatic RCS for the dielectric sphere in Fig. 2 computed using TENE-TH (2) ($f_E = 1,\ g_E = 1,\ f_H = -1,\ g_H = 0$) formulation as varying parameter κ.

κ	Δe_θ (mV)	Δe_ϕ (mV)	$\Delta\sigma$ (dBm^2)
0.3	6.0	5.0	0.41
0.4	4.8	5.7	0.34
0.5	4.1	6.4	0.30
0.6	4.0	6.8	0.29
0.7	4.5	6.9	0.31

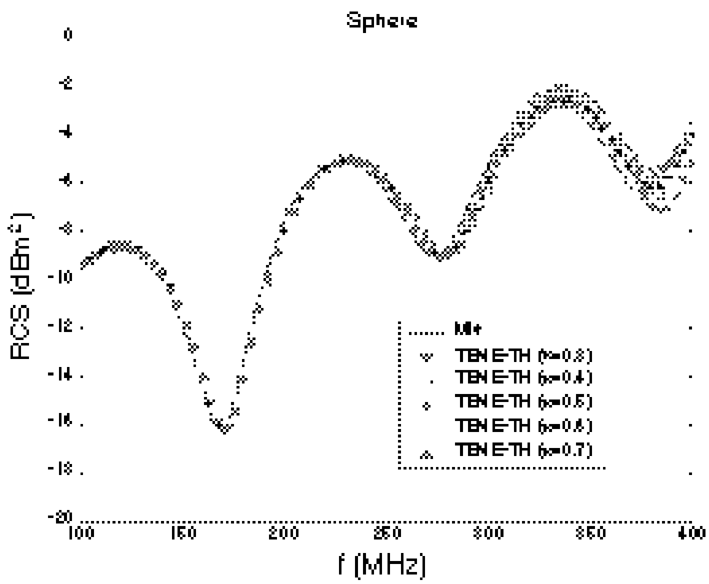

Figure 6. Monostatic RCS of the dielectric sphere in Fig. 2 computed by TENE-TH (2) formulation ($f_E = 1,\ g_E = 1,\ f_H = -1,\ g_H = 0$) as varying CFIE combining parameter κ.

Table 5. Seven CFIE formulations using different testing coefficients.

Formulation	f_E	g_E	f_H	g_H
TENE	1	1	0	0
THNH	0	0	-1	1
TENE-THNH	1	1	-1	1
TENE-TH	1	1	-1	0
TENE-NH	1	1	0	1
TE-THNH	1	0	-1	1
NE-THNH	0	1	-1	1

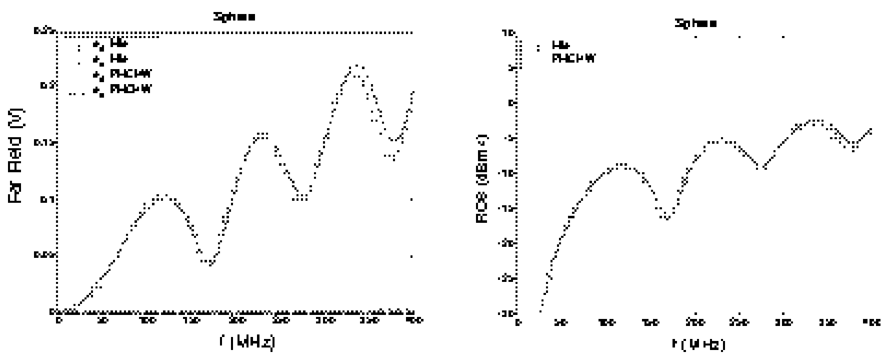

(a) Normalized far field (b) Monostatic RCS

Figure 7. PMCHW results for a dielectric sphere.

the results are calculated is $0 < f \leq 400\,\text{MHz}$ at an interval of 4 MHz. We compute the equivalent currents, the far field, and the monostatic RCS. We choose $\kappa = 0.5$ when CFIE is used. We compare all the computed equivalent currents with those obtained from the PMCHW formulation. Also, we compare the computed far fields and RCS with the Mie solution for a sphere and WIPL-D [10] solution for a cube and a cylinder. Mie and WIPL-D solutions are obtained at the same interval of 4 MHz.

As a first example, we consider the dielectric sphere of Fig. 2 used in the above section. The θ-directed electric current and the ϕ-directed magnetic current, as indicated by arrows in Fig. 2, are observed. Fig. 7

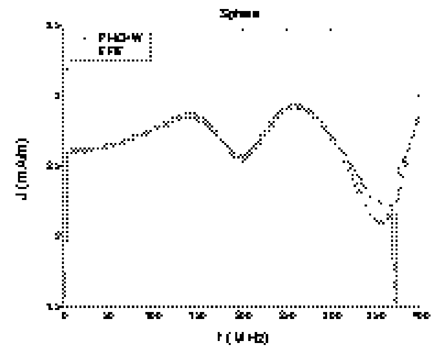

(a) Electric current

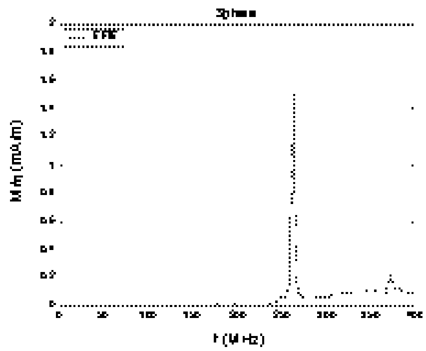

(b) Magnetic current

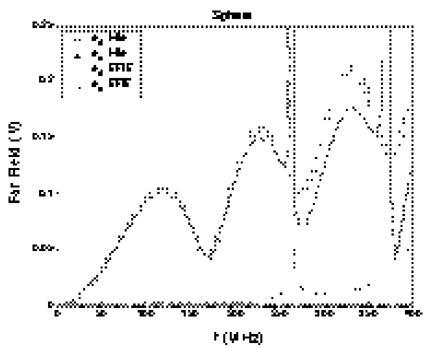

(c) Normalized far field

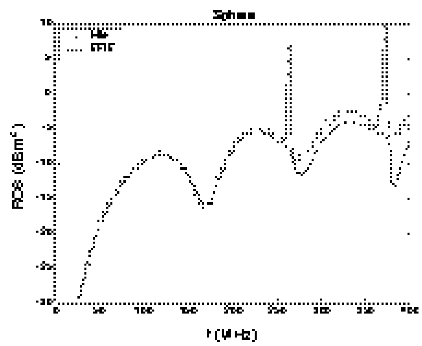

(d) Monostatic RCS

Figure 8. EFIE results for a dielectric sphere.

shows the results for the PMCHW. The far field and RCS agree well with Mie solution except for a small difference in the high frequency region. The currents are used to compare with any other numerical results and not shown here. Fig. 8 and Fig. 9 show the results of EFIE and MFIE obtained by using (41) and (47), respectively. Because the basis function for the magnetic current in the EFIE is different from that in PMCHW, we cannot compare together them in Fig. 8(b). Similarly, the basis function for the electric current in the MFIE is different from that in the PMCHW, hence we do not compare them in Fig. 9(a). The electric current in Fig. 8(a) and the magnetic current in Fig. 9(b) agree well with those of PMCHW except at the resonant frequencies. It is clearly seen that there are peaks and discontinuities

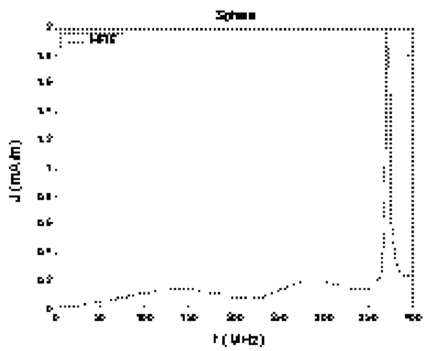

(a) Electric current

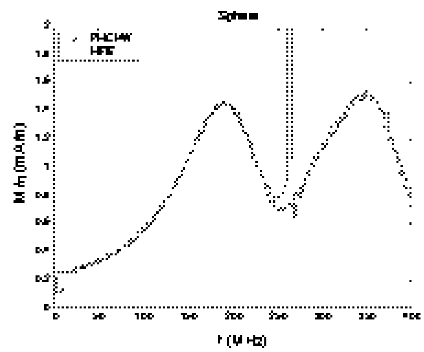

(b) Magnetic current

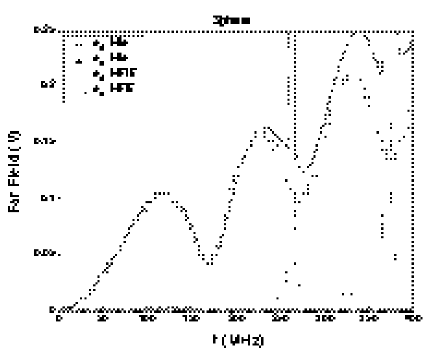

(c) Normalized far field

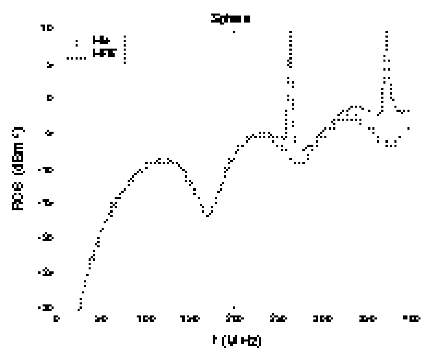

(d) Monostatic RCS

Figure 9. MFIE results for a dielectric sphere.

near the resonant frequencies of 262 and 369 MHz in the far field and RCS results.

Figures 10 and 11 show the numerical results for TENE and THNH, respectively. As discussed earlier, in Fig. 8 and Fig. 10 the results are presented using only the electric field and in Fig. 9 and Fig. 11 using only the magnetic field. For this reason, peaks at the resonant frequencies are observed in the figures. It is interesting to note that the electric current in the EFIE formulation and the magnetic current in the MFIE formulation agree better with the PMCHW solution than those of the TENE and THNH, even though $\underline{g}_m$ is used as expansion function for the magnetic current in EFIE and for the electric current in MFIE, which violates the property of

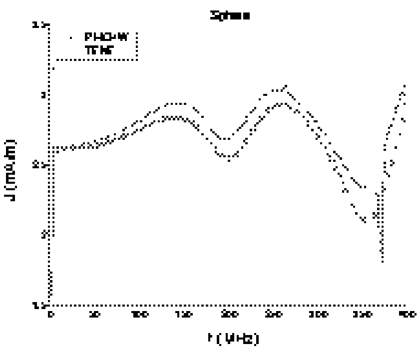

(a) Electric current

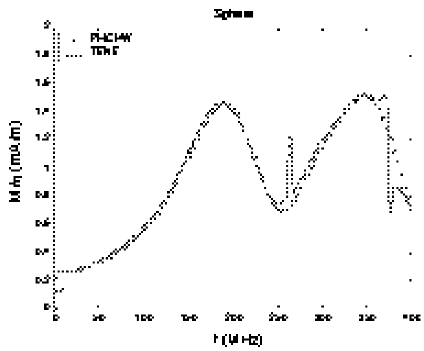

(b) Magnetic current

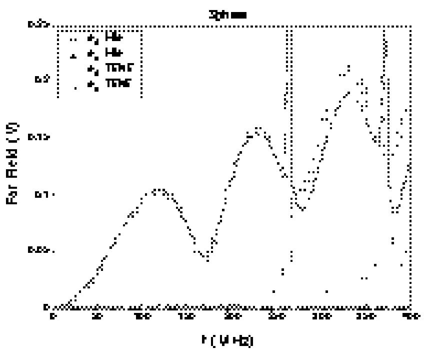

(c) Normalized far field

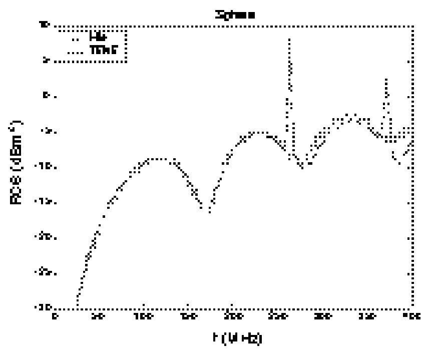

(d) Monostatic RCS

Figure 10. TENE results for a dielectric sphere ($f_E = 1,\ g_E = 1,\ f_H = 0,\ g_H = 0$).

each current. Fig. 12 gives the results computed by TENE-THNH, combining TENE and THNH formulation. In this CFIE, the resonant peaks or discontinuity in the plots are not seen. All the four figures in Fig. 12 check well with the PMCHW and Mie solution for the equivalent currents, the far fields, and RCS. The results of CFIE formulation when it neglects one term as discussed before are shown from Fig. 13 to Fig. 16. All numerical results do not show the resonant problem and agree well with the PMCHW solution for the currents and Mie solution for the far field and RCS exhibiting a small difference. But the results of TENE-TH are most accurate among them for both the far field and the RCS.

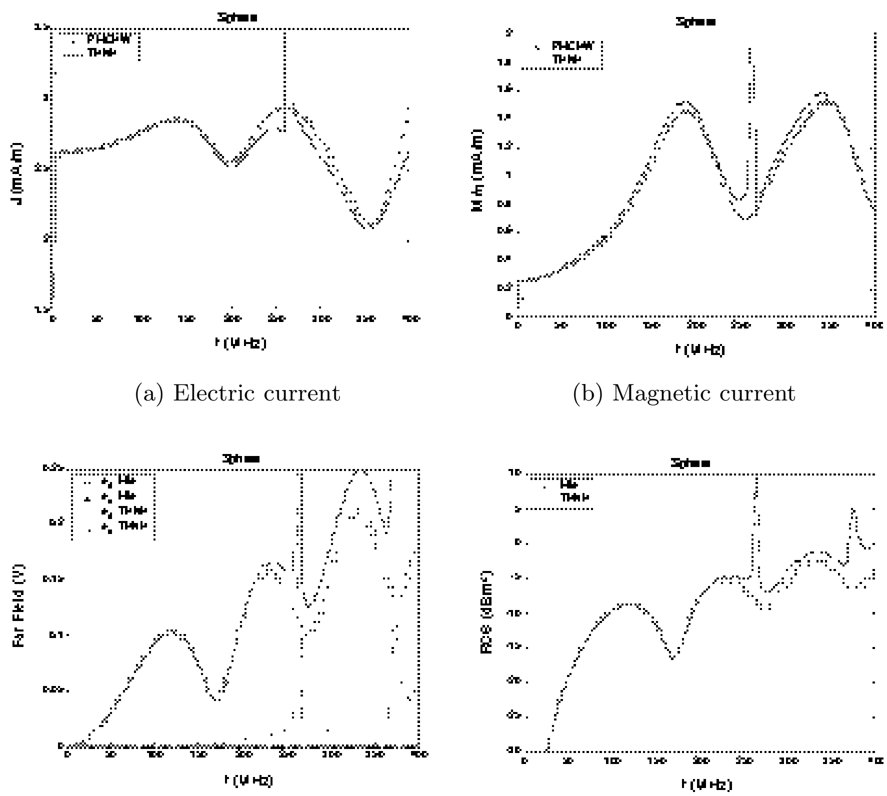

(a) Electric current

(b) Magnetic current

(c) Normalized far field

(d) Monostatic RCS

Figure 11. THNH results for a dielectric sphere ($f_E = 0,\ g_E = 0,\ f_H = -1,\ g_H = 1$).

Since the exact solution of the far field or RCS for a cube and a cylinder are not known, we use the code WIPL-D as a reference for comparison. To check the validity of this solution, we need to compare the solution from WIPL-D with the exact solution. Fig. 17 compares the WIPL-D and the Mie solutions for a sphere with a good agreement. The number of unknowns is 2,400 in the computation using WIPL-D. Table 6 summarizes the averaged difference of the normalized far field and monostatic RCS for the formulations which do not exhibit the resonant problem. From Table 6, we find that the TENE-NH has the smallest difference in the θ-component of the far field, but the difference in the ϕ-component of the far field is relatively large.

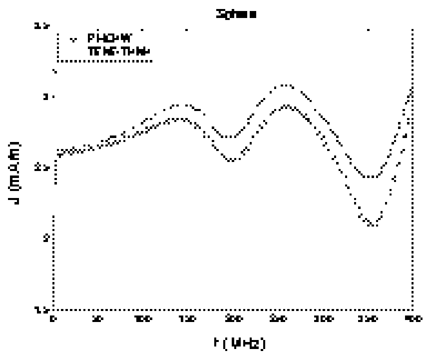

(a) Electric current

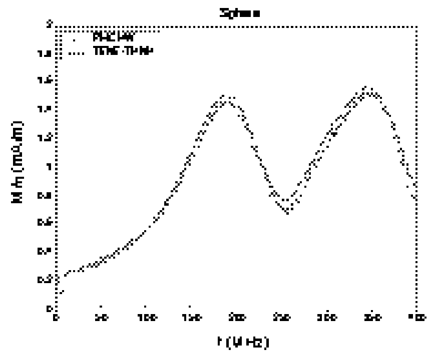

(b) Magnetic current

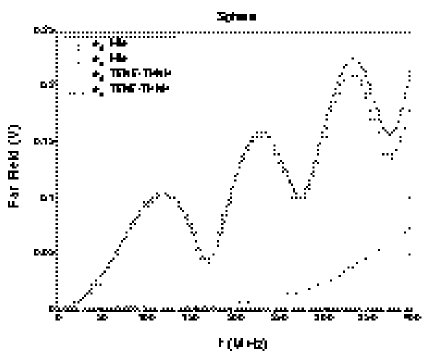

(c) Normalized far field

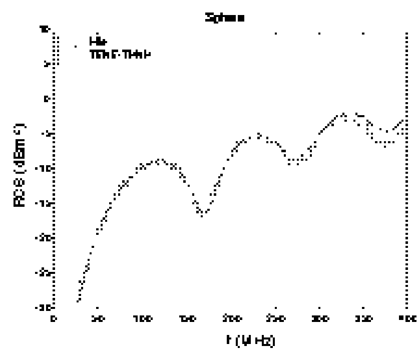

(d) Monostatic RCS

Figure 12. TENE-THNH results for a dielectric sphere ($f_E = 1,\ g_E = 1,\ f_H = -1,\ g_H = 1$).

As a second example, we consider a dielectric cube, 1 m on a side, centered about the origin shown in Fig. 18. There are eight divisions along each direction, respectively. This results in a total of 768 patches and 1,152 edges. The z-directed electric current and the y-directed magnetic current, as indicated by arrows on a side face of the cube in Fig. 18, are observed. The computed currents are compared with those of the PMCHW formulation and the far fields and the monostatic RCS are compared with the WIPL-D solutions. The number of unknowns is 2,400 in the computation using WIPL-D.

Fig. 19 shows the results of PMCHW. The far field and the RCS agree well with WIPL-D solutions in the entire frequency region.

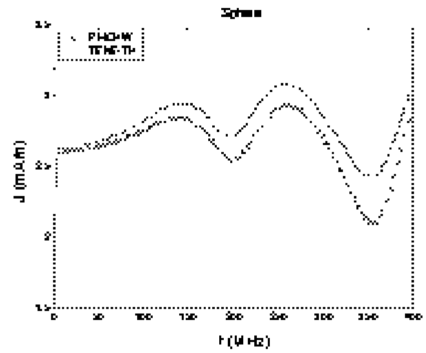

(a) Electric current

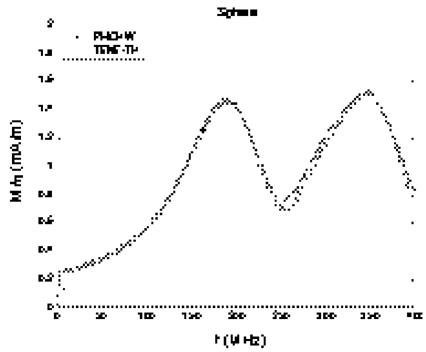

(b) Magnetic current

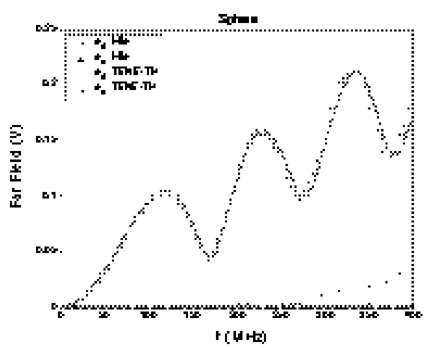

(c) Normalized far field

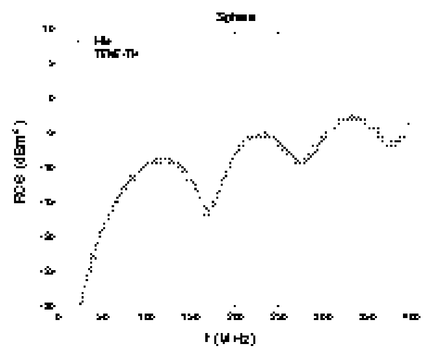

(d) Monostatic RCS

Figure 13. TENE-TH results for a dielectric sphere ($f_E = 1,\ g_E = 1,\ f_H = -1,\ g_H = 0$).

Figures 20 and 21 show the results for EFIE and MFIE, respectively. The basis function of the magnetic currents in the EFIE is different from that in PMCHW, and so we cannot compare them in Fig. 20(b). Similarly, the basis function of the electric currents in the MFIE is different from that in PMCHW, and therefore we do not compare them in Fig. 21(a). The electric current in Fig. 20(a) and the magnetic current in Fig. 21(b) agree well with those of PMCHW except near resonant frequencies 212, 335, and 367 MHz. It is clearly seen that there are discontinuities at the resonant frequencies in the far field and RCS.

Figures 22 and 23 show the numerical results for TENE and

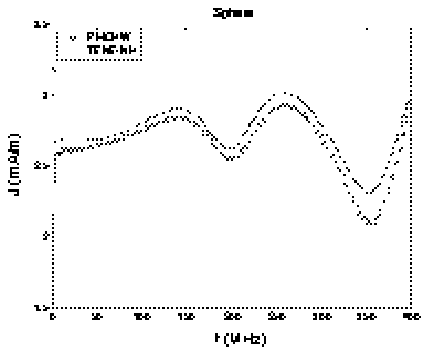

(a) Electric current

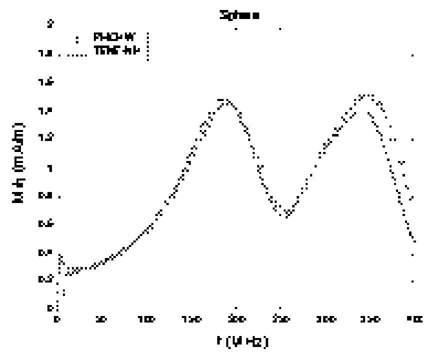

(b) Magnetic current

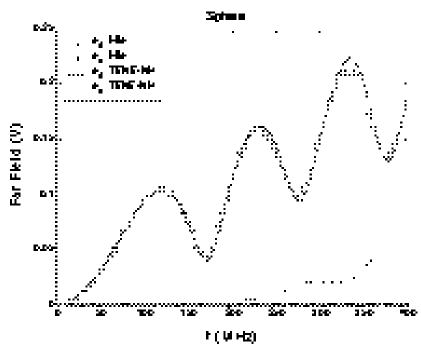

(c) Normalized far field

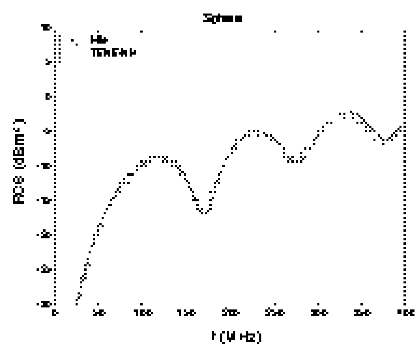

(d) Monostatic RCS

Figure 14. TENE-NH results for a dielectric sphere ($f_E = 1,\ g_E = 1,\ f_H = 0,\ g_H = 1$).

THNH, respectively. As discussed earlier, Figures 20 and 22 are results derived from only the electric field and Figures 21 and 23 are results derived from only the magnetic field. For this reason, spurious peaks in the solutions are observed at the internal resonant frequencies. It is interesting to note that the electric current for the EFIE and the magnetic current for the MFIE agree well with the PMCHW solution than those of TENE and THNH, even though $\underline{g}_m$ is used as expansion function for the magnetic current in EFIE and for the electric current in MFIE formulations, which violate the property of the currents. Fig. 24 presents the results computed by TENE-THNH, by combining the TENE and THNH formulation. In this CFIE, the resonant peak or

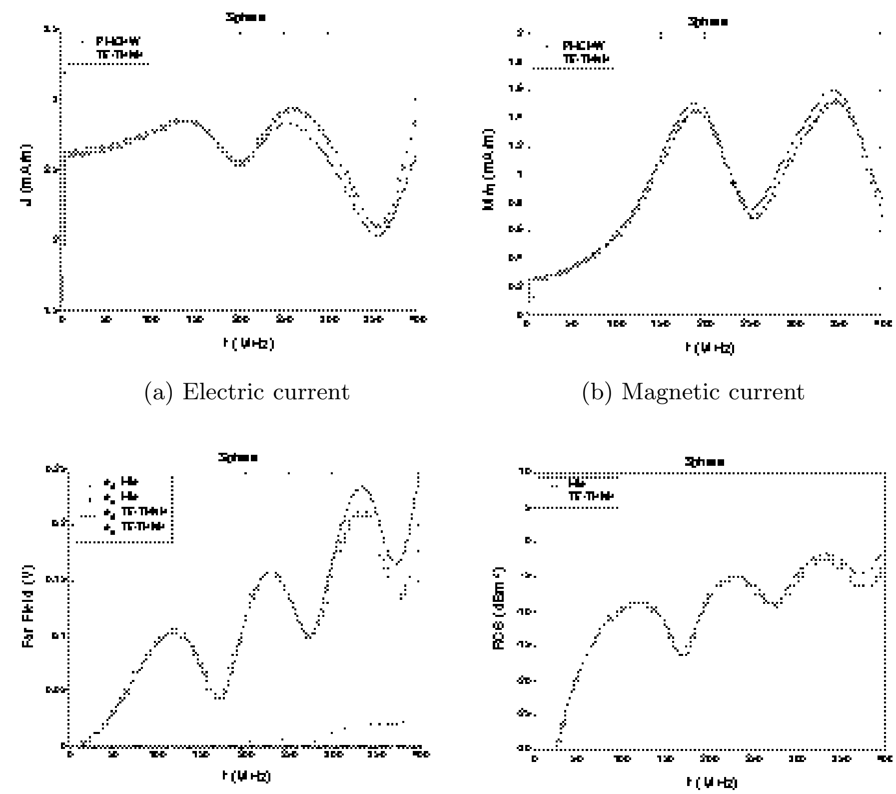

(a) Electric current

(b) Magnetic current

(c) Normalized far field

(d) Monostatic RCS

Figure 15. TE-THNH results for a dielectric sphere ($f_E = 1,\ g_E = 0,\ f_H = -1,\ g_H = 1$).

discontinuity is not seen. The four figures in Fig. 24 agree well with the PMCHW formulation for the equivalent currents and the WIPL-D solution for the far field and RCS. The results of the CFIE with one term dropped are shown in Figures 25 to 28. All numerical results do not exhibit the resonant problem and agree well with the PMCHW formulation for the currents and the WIPL-D solution for the far field and RCS even though there is a small difference. It is important to note that the magnetic current of the TENE-TH shows an excellent agreement with the PMCHW solution in Fig. 25(b). Also the far field and RCS of the TENE-NH in Fig. 26(c) and (d) are the most accurate. Table 7 summarizes the averaged difference between the normalized

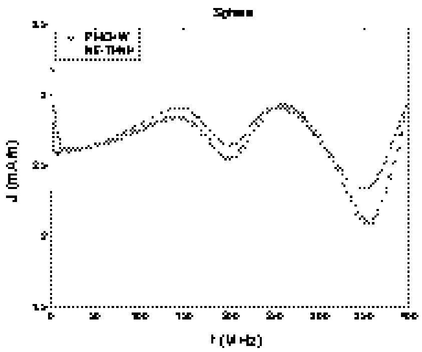

(a) Electric current

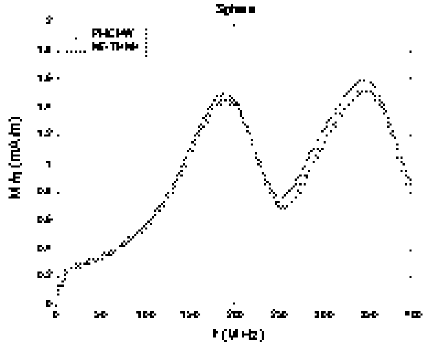

(b) Magnetic current

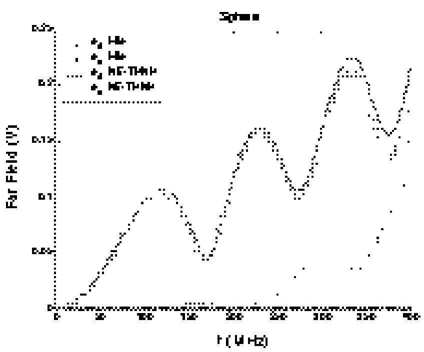

(c) Normalized far field

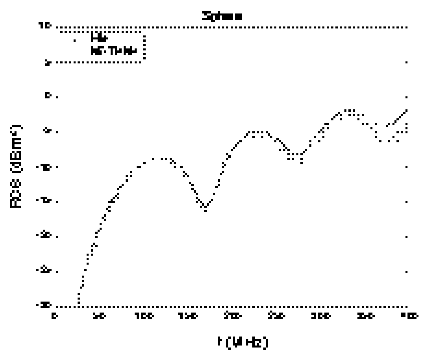

(d) Monostatic RCS

Figure 16. NE-THNH results for a dielectric sphere ($f_E = 0,\ g_E = 1,\ f_H = -1,\ g_H = 1$).

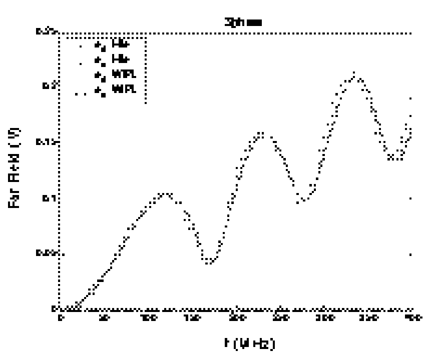

(a) Normalized far field

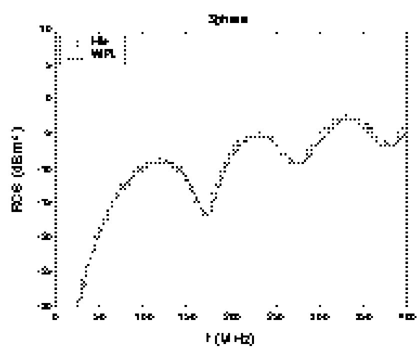

(b) Monostatic RCS

Figure 17. WIPL results for a dielectric sphere.

Table 6. Averaged difference of the normalized far field and monostatic RCS between Mie and the numerical solution for the dielectric sphere in Fig. 2.

Formulation	Δe_θ (mV)	Δe_ϕ (mV)	$\Delta\sigma$ (dBm^2)
PMCHW	4.7	0.8	0.34
TENE-THNH	5.3	16.1	0.40
TENE-TH	4.1	6.4	0.30
TENE-NH	3.5	12.9	0.28
TE-THNH	8.7	7.2	0.55
NE-THNH	5.7	21.5	0.52
WIPL	0.1	0.1	0.42

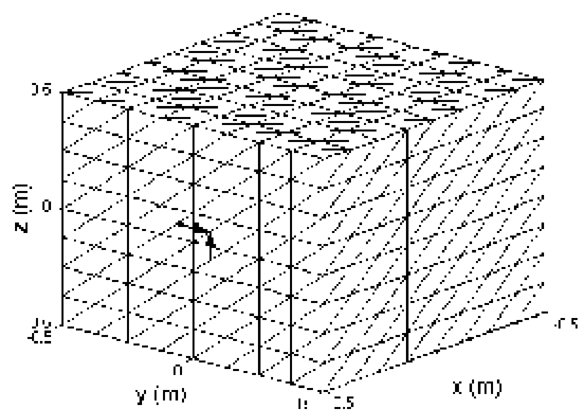

Figure 18. Triangle surface patching of a dielectric cube (side 1 m). z- and y-directed arrows represent position and direction of sampled currents $\underline{J}$ and $\underline{M}$, respectively.

far field and the monostatic RCS for the PMCHW and five different CFIE formulations. If we look at Table 7, TENE-NH has the smallest difference in both θ- and ϕ-component of the far field and RCS.

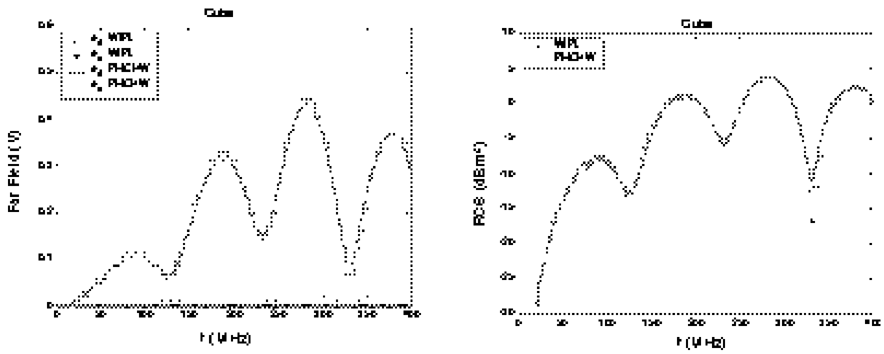

(a) Normalized far field (b) Monostatic RCS

Figure 19. PMCHW results for a dielectric cube.

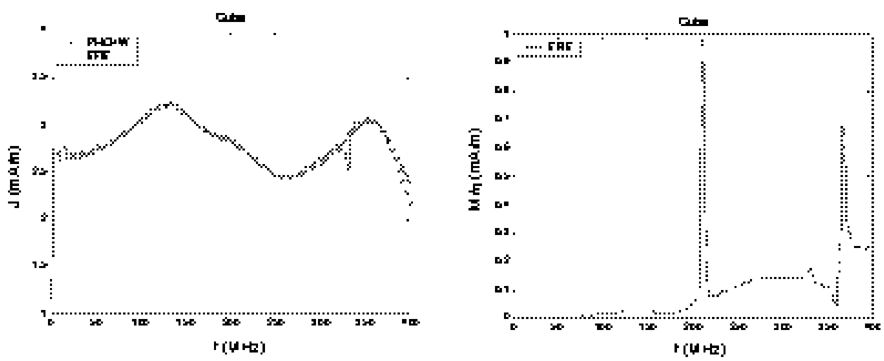

(a) Electric current (b) Magnetic current

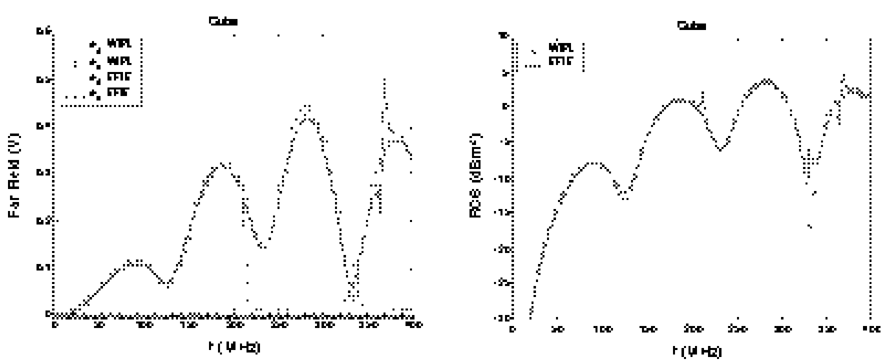

(c) Normalized far field (d) Monostatic RCS

Figure 20. EFIE results for a dielectric cube.

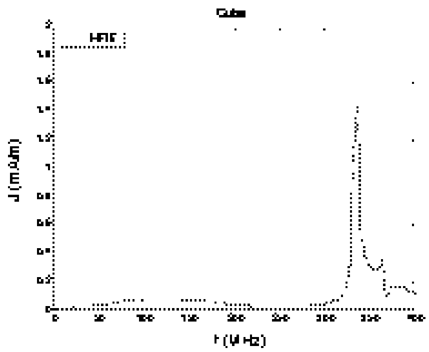

(a) Electric current

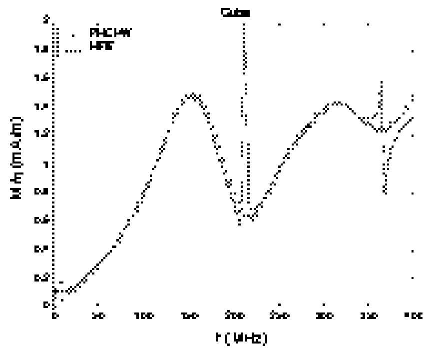

(b) Magnetic current

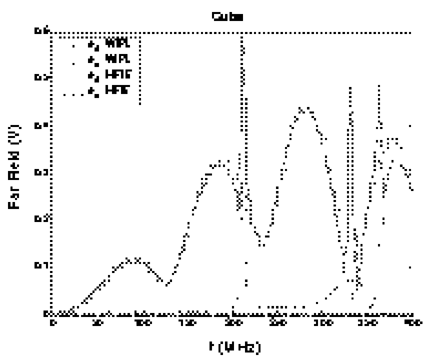

(c) Normalized far field

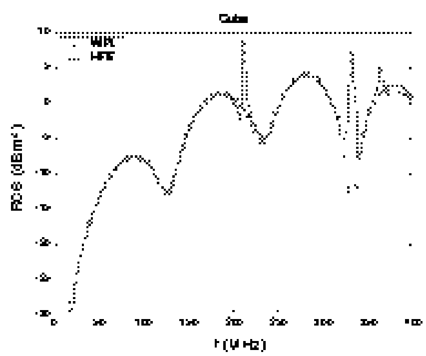

(d) Monostatic RCS

Figure 21. MFIE results for a dielectric cube.

Table 7. Averaged difference of the normalized far field and monostatic RCS between WIPL-D and numerical solution for the dielectric cube in Fig. 18.

Formulation	Δe_θ (mV)	Δe_ϕ (mV)	$\Delta\sigma$ (dBm^2)
PMCHW	8.2	10.9	0.65
TENE-THNH	9.5	23.7	0.50
TENE-TH	11.6	16.3	0.59
TENE-NH	6.4	9.5	0.35
TE-THNH	9.0	20.1	0.52
NE-THNH	12.0	18.1	0.68

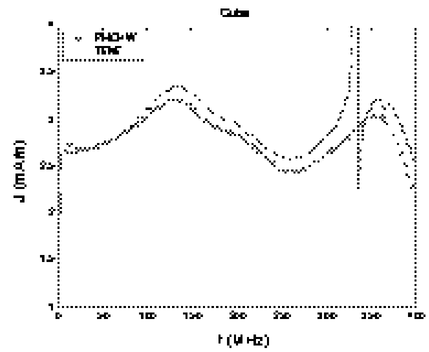

(a) Electric current

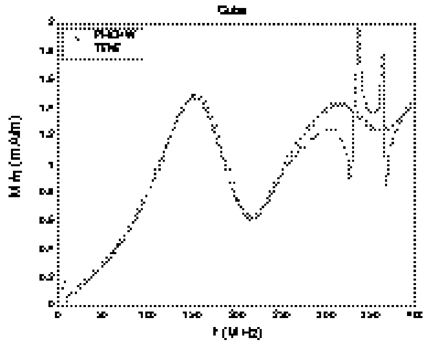

(b) Magnetic current

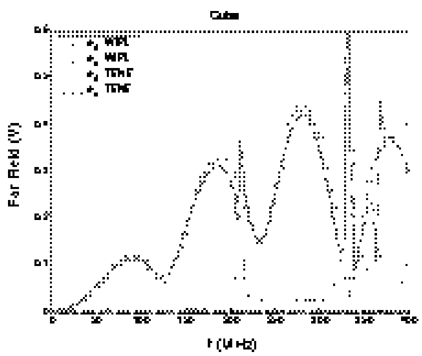

(c) Normalized far field

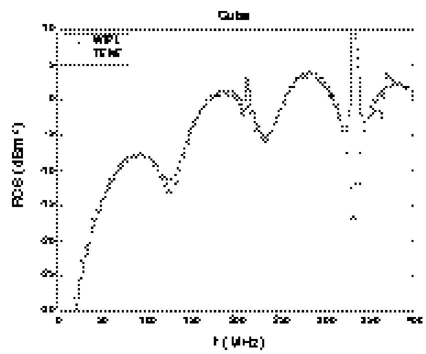

and (d) Monostatic RCS

Figure 22. TENE results for a dielectric cube ($f_E = 1,\ g_E = 1,\ f_H = 0,\ g_H = 0$).

As a final example, we present the numerical results for a finite dielectric cylinder with a radius of 0.5 m and a height 1 m, centered at the origin, as shown in Fig. 29. We subdivide the cylinder into four, twenty-four, and eight divisions along r, ϕ, and z directions, respectively. This represents a total of 720 patches with 1,080 edges. The z-directed electric current and the ϕ-directed magnetic current are observed at a location indicated by the arrows in Fig. 29. The computed currents are compared with those of the PMCHW and the far fields and monostatic RCS are compared with the WIPL-D solution. The number of unknowns is 2,688 in the computation using WIPL-D.

Fig. 30 shows the results for the PMCHW. The far field and RCS

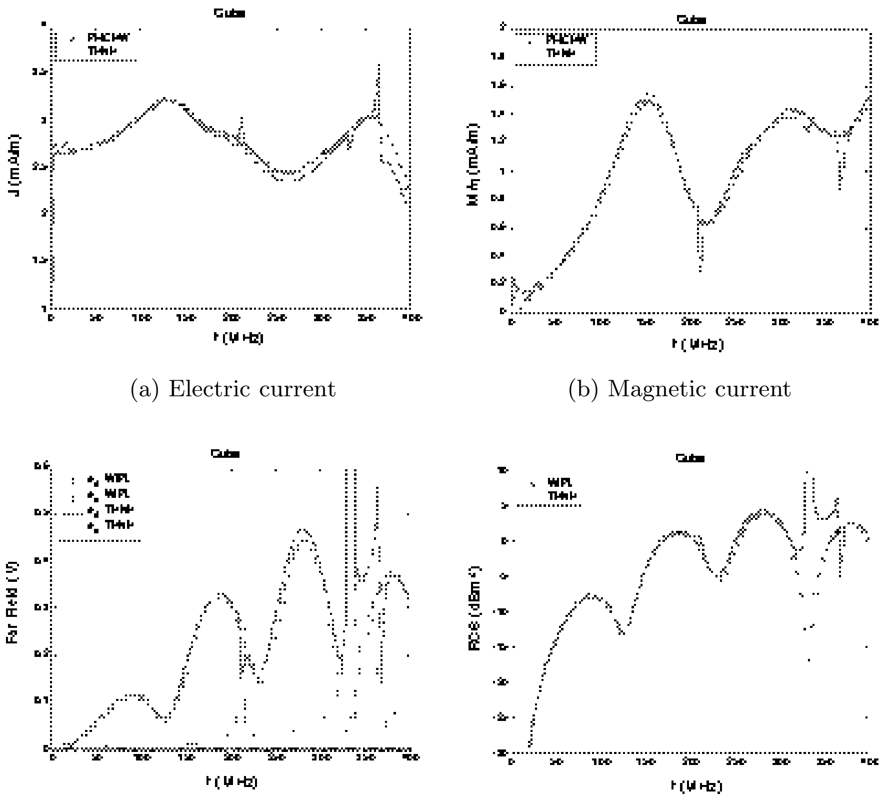

(a) Electric current (b) Magnetic current

(c) Normalized far field (d) Monostatic RCS

Figure 23. THNH results for a dielectric cube ($f_E = 0,\ g_E = 0,\ f_H = -1,\ g_H = 1$).

agree well with the WIPL-D solution in the entire frequency region. Figs. 31 and 32 show the results of EFIE and MFIE, respectively. The basis function for the magnetic currents in EFIE is different from that in the PMCHW, and so we do not compare them in Fig. 31(b). Similarly, the basis function of the electric currents in the MFIE is different from that in the PMCHW, and so we do not compare them in Fig. 32(a). The electric current in Fig. 31(a) and the magnetic current in Fig. 32(b) agree well with those of the PMCHW except at the resonant frequencies. It is clearly seen that there are discontinuities in the figures near the resonant frequencies 230, 328, and 366 MHz in the far field and RCS.

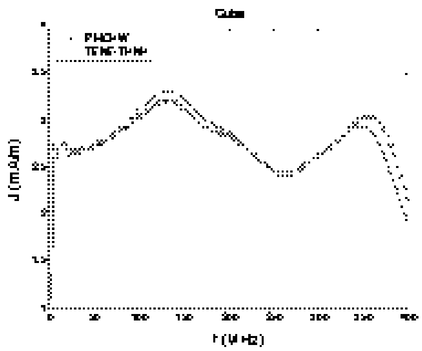

(a) Electric current

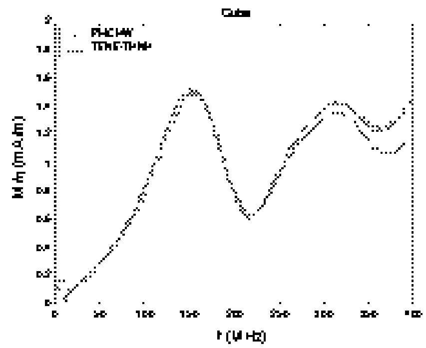

(b) Magnetic current

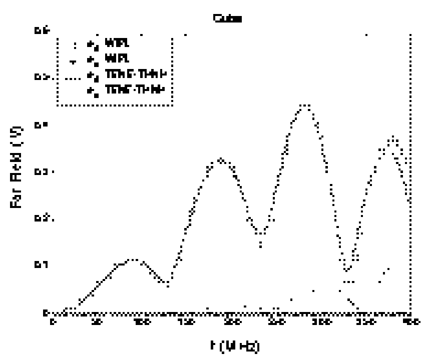

(c) Normalized far field

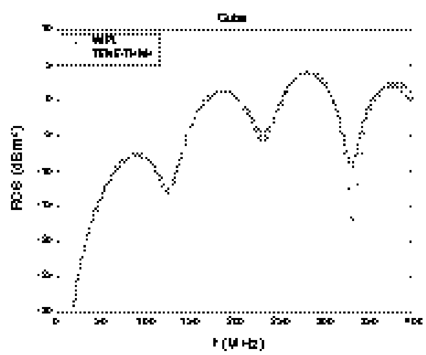

(d) Monostatic RCS

Figure 24. TENE-THNH results for a dielectric cube ($f_E = 1,\ g_E = 1,\ f_H = -1,\ g_H = 1$).

Figures 33 and 34 show the numerical results of TENE and THNH, respectively. Figures 31 and 33 are the results derived from only the electric field and Figures 32 and 34 are results derived from only the magnetic field. For this reason, spurious peaks in the solution are observed at the resonant frequencies. It is interesting to note that the electric current for the EFIE and the magnetic current for the MFIE formulation agree well with the PMCHW solution than those of TENE and THNH, even though $\underline{g}_m$ is used as expansion function for the magnetic current in the EFIE and the electric current in the MFIE formulations, which is not the appropriate expansion function for each current. Fig. 35 shows the results computed by TENE-THNH,

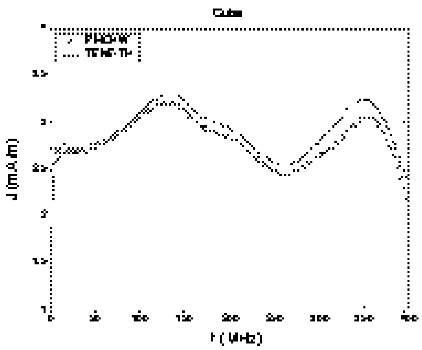

(a) Electric current

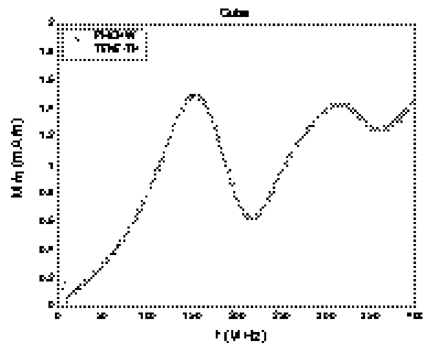

(b) Magnetic current

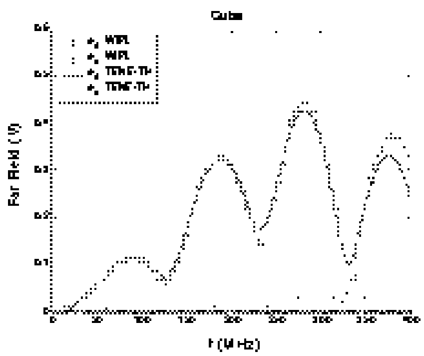

(c) Normalized far field

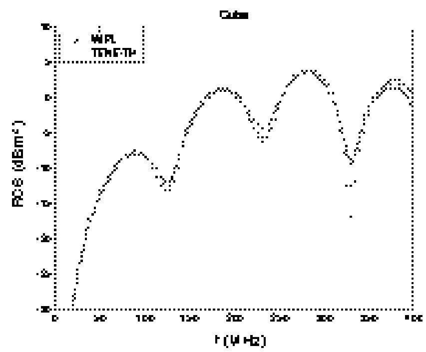

(d) Monostatic RCS

Figure 25. TENE-TH results for a dielectric cube ($f_E = 1,\ g_E = 1,\ f_H = -1,\ g_H = 0$).

by combining the TENE and the THNH formulation. For this CFIE, the spurious resonant peaks are not seen. All the four figures in Fig. 35 check well with PMCHW and WIPL-D solutions. The results of the CFIE formulation with one term neglected are shown from Figures 36 to 39. All of the numerical results do not exhibit the spurious resonant peaks and agree well with the PMCHW for the currents and the WIPL-D solution for the far field and RCS. Table 8 summarizes the averaged differences of the normalized far field and the monostatic RCS for PMCHW and five CFIE formulations. If we look carefully at Table 8, except for the PMCHW, we observe that TENE-THNH has a small difference in the θ-component of the far field, yet the difference in the ϕ-component of the far field is relatively large. If we consider the

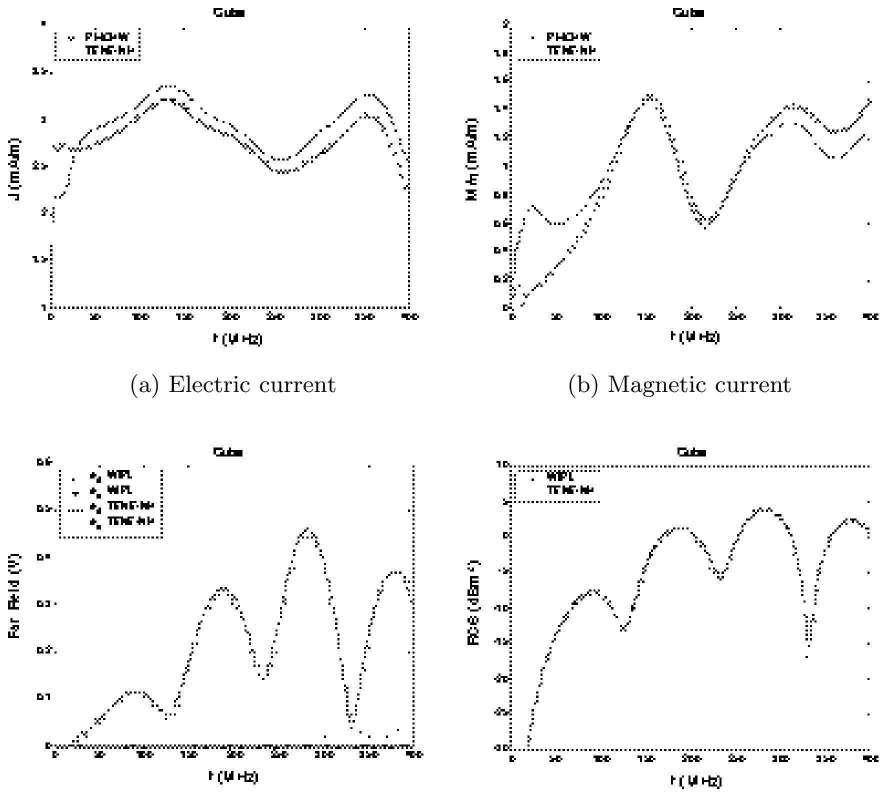

(a) Electric current (b) Magnetic current

(c) Normalized far field (d) Monostatic RCS

Figure 26. TENE-NH results for a dielectric cube ($f_E = 1,\ g_E = 1,\ f_H = 0,\ g_H = 1$).

averaged difference of both the far field and RCS, TENE-NH seems to be the most accurate.

6. CONCLUSION

A set of coupled integral equations is used to analyze scattering from 3-D dielectric objects. The integral equation formulations are derived using the equivalence principle and utilizing the continuity conditions on the fields. To obtain a numerical solution, we employ the MoM in conjunction with the planar triangular patch basis function. The EFIE and MFIE formulations give valid solutions except at frequencies, which correspond to an internal resonant frequency of the scatterer, are

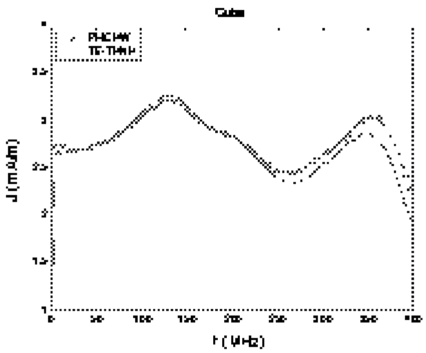

(a) Electric current

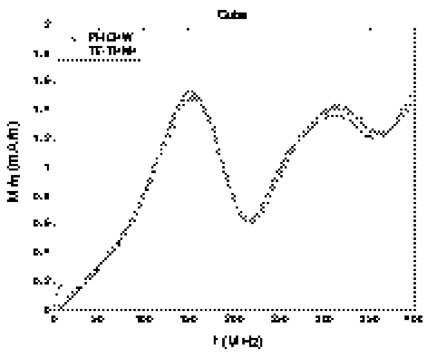

(b) Magnetic current

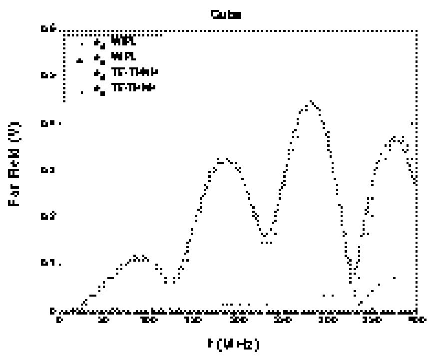

(c) Normalized far field

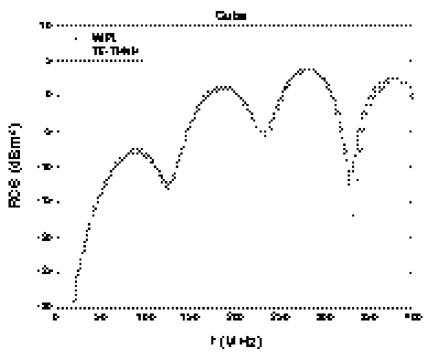

(d) Monostatic RCS

Figure 27. TE-THNH results for a dielectric cube ($f_E = 1,\ g_E = 0,\ f_H = -1,\ g_H = 1$).

compared with two other formulations TENE and THNH, which also exhibit resonance problems. In order to obtain CFIE, we introduce four testing coefficients in the combination of the TENE and THNH. As a result, we have eight different cases of the CFIE formulation of which only two formulations are not affected by internal resonances. We also present sixteen possible cases of the CFIE by dropping one of terms in the testing and check to see if all the sixteen formulations give valid solutions. The important point to note is that not all possible CFIE formulations eliminate the internal resonance problem. When we use CFIE with other formulations, for example, to analyze scattering from composite structures with conductors and dielectrics, TENE-THNH, TENE-TH, or TENE-NH may be used.

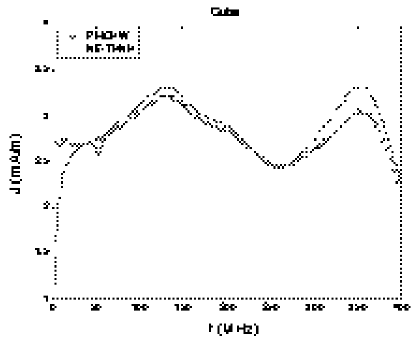

(a) Electric current

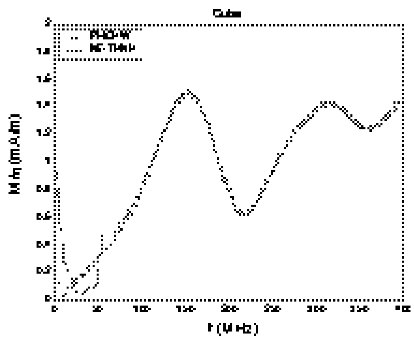

(b) Magnetic current

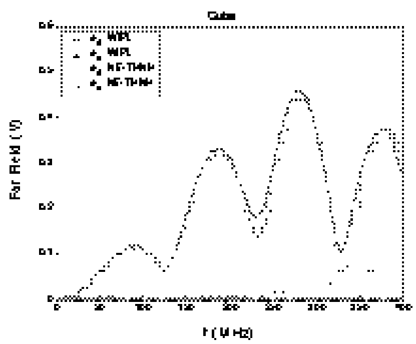

(c) Normalized far field

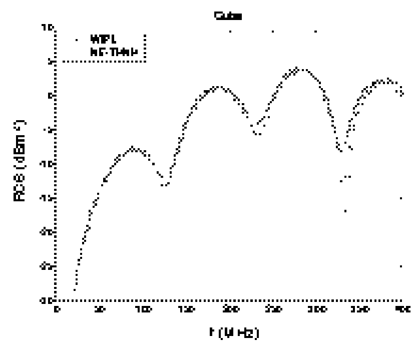

(d) Monostatic RCS

Figure 28. NE-THNH results for a dielectric cube ($f_E = 0,\ g_E = 1,\ f_H = -1,\ g_H = 1$).

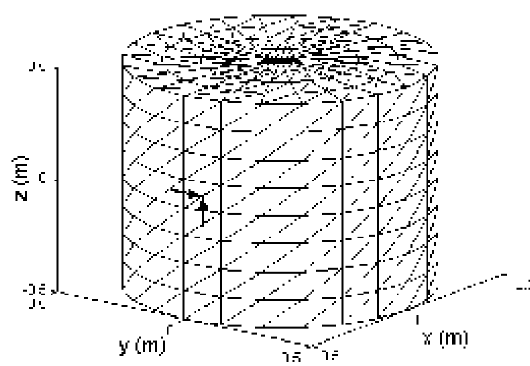

Figure 29. Triangle surface patching of a dielectric cylinder (radius 0.5 m and height 1 m). z- and ϕ-directed arrows represent position and direction of sampled currents $\underline{J}$ and $\underline{M}$, respectively.

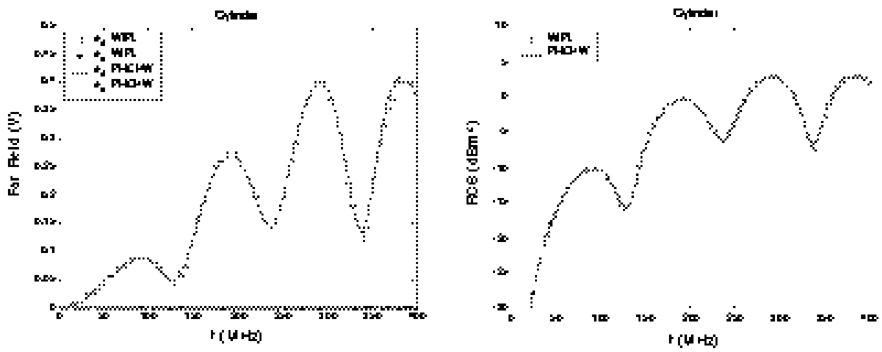

(a) Normalized far field (b) Monostatic RCS

Figure 30. PMCHW results for a dielectric cylinder.

Table 8. Averaged difference of the normalized far field and monostatic RCS between WIPL-D and numerical solution for the dielectric cylinder in Fig. 29.

Formulation	Δe_θ (mV)	Δe_ϕ (mV)	$\Delta\sigma$ (dBm^2)
PMCHW	3.7	1.5	0.35
TENE-THNH	5.8	16.9	0.47
TENE-TH	7.4	10.6	0.55
TENE-NH	9.7	11.5	0.47
TE-THNH	7.5	13.0	0.55
NE-THNH	15.7	18.5	0.78

APPENDIX A.

In this Appendix, it is shown how to evaluate some of the integrals. We drop the subscript v representing the medium. Note that while computing the elements of the matrix, the appropriate material parameters should be included in evaluating the integrals.

A.1. Integrals (26), (73), and (74)

First, we consider the integral (26). Substituting (17) into (26), we get four terms. We define the summation operator as

$$A_{mn} = A_{mn}^{++} + A_{mn}^{+-} + A_{mn}^{-+} + A_{mn}^{--} \equiv \sum_{p,q} A_{mn}^{pq} \tag{A1}$$

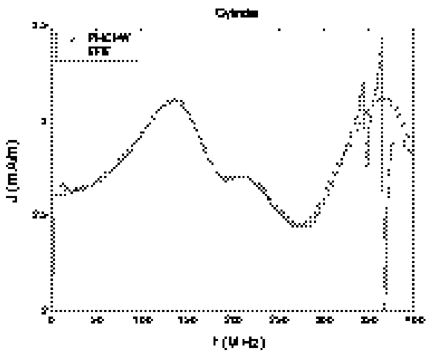

(a) Electric current

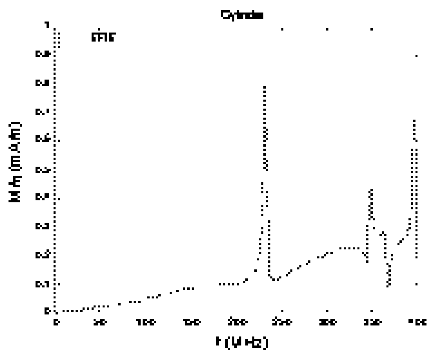

(b) Magnetic current

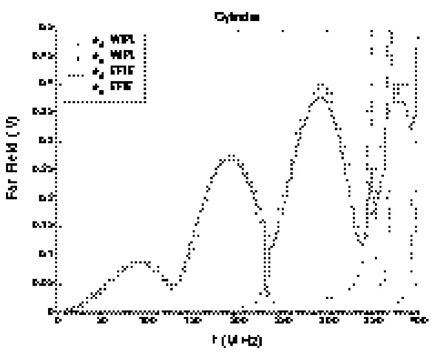

(c) Normalized far field

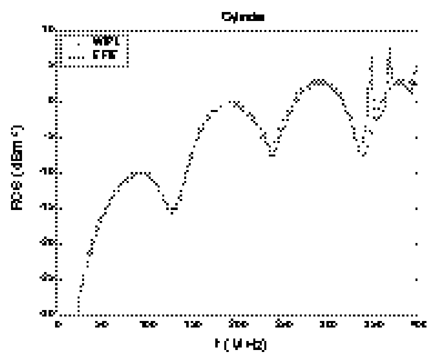

(d) Monostatic RCS

Figure 31. EFIE results for a dielectric cylinder.

where

$$A_{mn}^{pq} = \frac{1}{4\pi} \int_S \underline{f}_m^p(\underline{r}) \cdot \int_S \underline{f}_n^q(\underline{r}') G(\underline{r}, \underline{r}') dS' dS \tag{A2}$$

and p and q can be either $+$ or $-$. If the integral on the unprimed variable is evaluated by approximating the integrand by the respective values at the centroid of the testing triangle T_m^p, (A2) becomes

$$A_{mn}^{pq} = \frac{l_m l_n}{16\pi} \underline{\rho}_m^{cp} \cdot \frac{1}{A_n^q} \int_{T_n^q} \underline{\rho}_n^q \frac{e^{-jkR_m^p}}{R_m^p} dS' \tag{A3}$$

where

$$R_m^p = |\underline{r}_m^{cp} - \underline{r}'| \tag{A4}$$

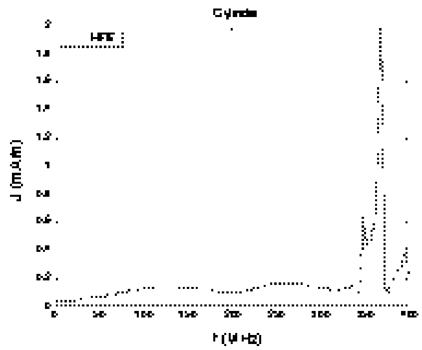

(a) Electric current

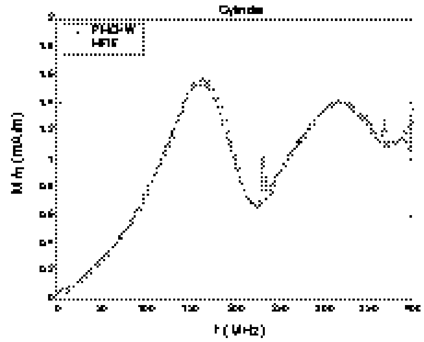

(b) Magnetic current

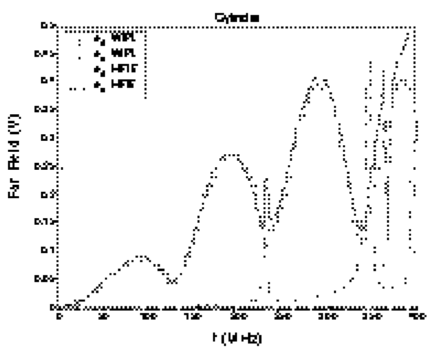

(c) Normalized far field

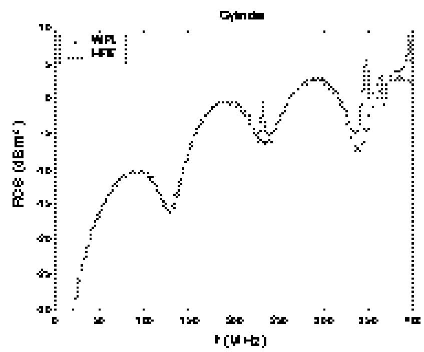

(d) Monostatic RCS

Figure 32. MFIE results for a dielectric cylinder.

and $\underline{r}_m^{cp}$ is the position vector of the centeroid of the triangle T_m^p. Equation (73) is same as (26) or (A1), and (74) may be evaluated by replacing $\underline{\rho}_m^{cp}$ with $\hat{n} \times \underline{\rho}_m^{cp}$ in (A3).

A.2. Integrals (29), (75), and (76)

By substituting (18) into (29), we get

$$B_{mn} = B_{mn}^{++} + B_{mn}^{+-} + B_{mn}^{-+} + B_{mn}^{--} \equiv \sum_{p,q} B_{mn}^{pq} \tag{A5}$$

where

$$B_{mn}^{pq} = \frac{1}{4\pi} \int_S \nabla_S \cdot \underline{f}_m^p(\underline{r}) \int_S \nabla'_S \cdot \underline{f}_n^q(\underline{r}') G(\underline{r}, \underline{r}') dS' dS. \tag{A6}$$

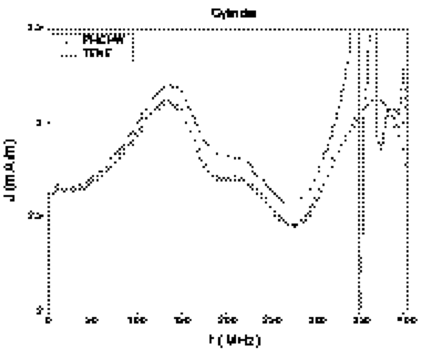

(a) Electric current

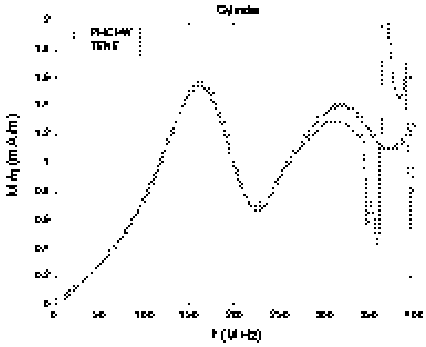

(b) Magnetic current

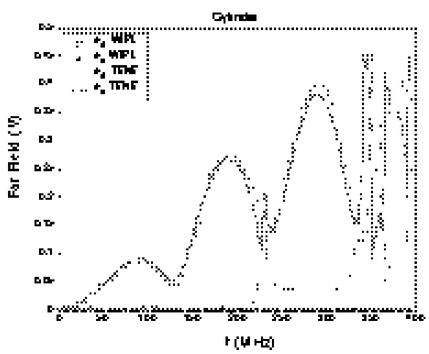

(c) Normalized far field

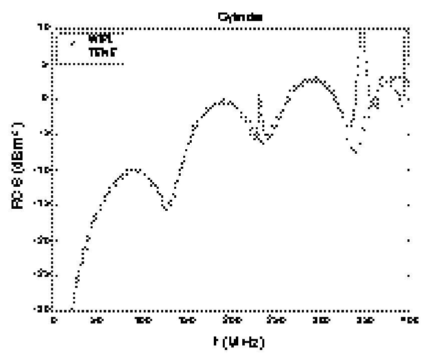

and (d) Monostatic RCS

Figure 33. TENE results for a dielectric cylinder ($f_E = 1$, $g_E = 1$, $f_H = 0$, $g_H = 0$).

Approximating the integrand by the respective values at the centroid of the testing triangle T_m^p, (A6) becomes

$$B_{mn}^{pq} = \frac{l_m l_n}{4\pi} \frac{1}{A_n^q} \int_{T_n^q} \frac{e^{-jkR_m^p}}{R_m^p} dS' \tag{A7}$$

where R_m^p is given by (A4). Equation (75) is same as (18) or (A5). Equation (76) is evaluated through

$$B_{mn}^g = \sum_{p,q} B_{mn}^{pq,g} \tag{A8}$$

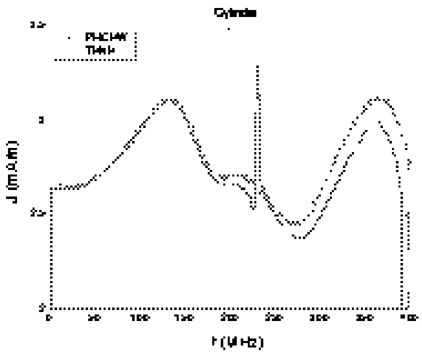

(a) Electric current

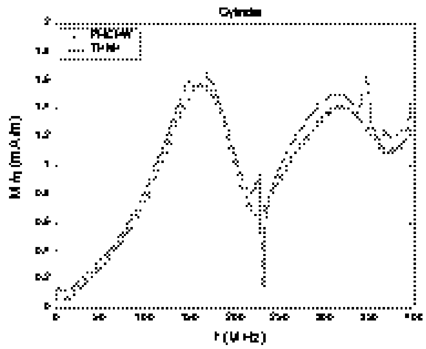

(b) Magnetic current

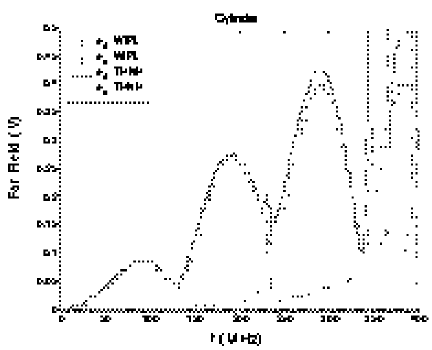

(c) Normalized far field

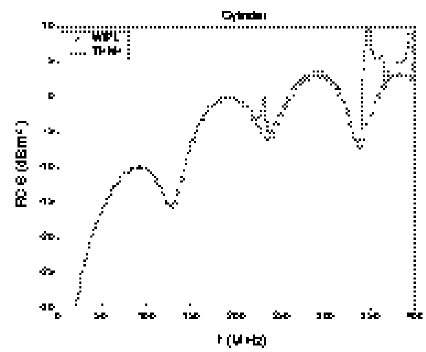

(d) Monostatic RCS

Figure 34. THNH results for a dielectric cylinder ($f_E = 0$, $g_E = 0$, $f_H = -1$, $g_H = 1$).

where

$$B_{mn}^{pq,g} = \frac{1}{4\pi}\int_S \hat{n}\times \underline{f}_m^p(\underline{r})\cdot\int_S \nabla'_S\cdot\underline{f}_n^q(\underline{r}')\nabla' G(\underline{r},\underline{r}')dS'dS. \qquad \text{(A9)}$$

Approximating the integrand by the respective values at the centroid of the testing triangle T_m^p, (A9) becomes

$$B_{mn}^{pq,g} = \frac{l_m l_n}{8\pi}\hat{n}\times\underline{\rho}_m^p\cdot\frac{1}{A_n^q}\int_{T_n^q}\nabla'\frac{e^{-jkR_m^p}}{R_m^p}dS' \qquad \text{(A10)}$$

The evaluation of the potential integrals in (A3), (A7), and (A10) may be carried out by using the numerical methods specially developed for triangular regions in [11–14].

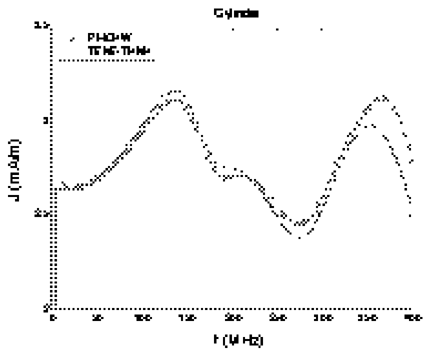

(a) Electric current

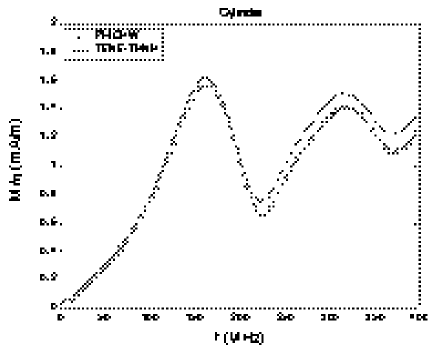

(b) Magnetic current

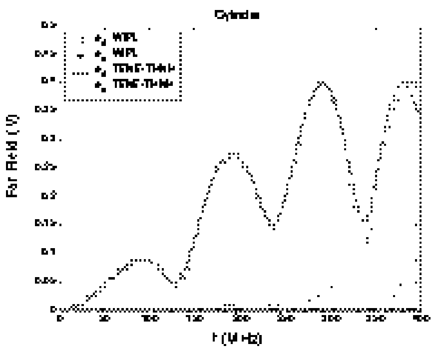

(c) Normalized far field

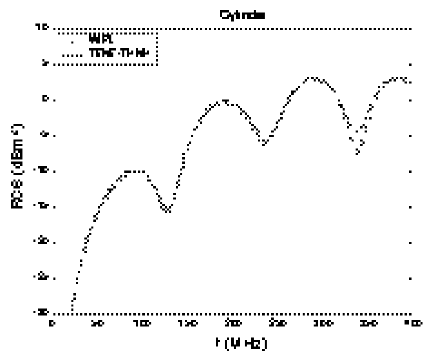

and (d) Monostatic RCS

Figure 35. TENE-THNH results for a dielectric cylinder ($f_E = 1,\ g_E = 1,\ f_H = -1,\ g_H = 1$).

A.3. Integrals (35), (77), and (78)

Using a vector identity [8], (35) is given by

$$C_{mn} = \frac{1}{2}\int_S \underline{f}_m(\underline{r}) \cdot \hat{n} \times \{\hat{n} \times \underline{f}_n(\underline{r})\} dS = -\sum_{p,q} \frac{1}{2}\int_S \underline{f}_m^p \cdot \underline{f}_n^q dS. \quad \text{(A11)}$$

The integral of (A11) can be computed analytically and the result is given by [9]

$$\frac{1}{2}\int_S \underline{f}_m^p \cdot \underline{f}_n^q dS \;=\; \pm\frac{l_m l_n}{8A}\left\{\frac{3}{4}|\underline{r}_c|^2 + \frac{1}{12}(|\underline{r}_1|^2 + |\underline{r}_2|^2 + |\underline{r}_3|^2)\right.$$

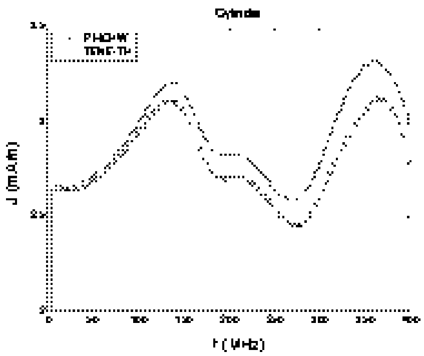

(a) Electric current

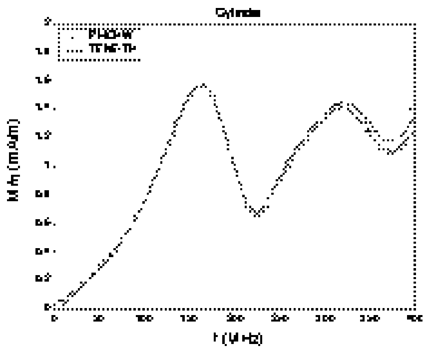

(b) Magnetic current

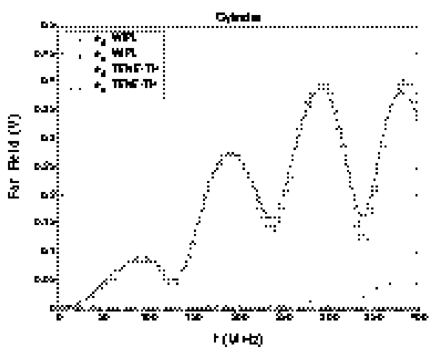

(c) Normalized far field

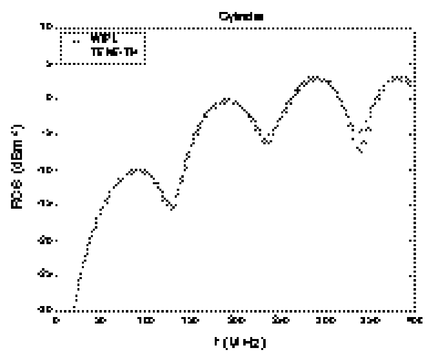

(d) Monostatic RCS

Figure 36. TENE-TH results for a dielectric cylinder ($f_E = 1,\ g_E = 1,\ f_H = -1,\ g_H = 0$).

$$\left.-\underline{r}^c \cdot (\underline{r}_m + \underline{r}_n) + \underline{r}_m \cdot \underline{r}_n\right\} \tag{A12}$$

where $\underline{r}_1,\ \underline{r}_2$, and $\underline{r}_3$ are the position vectors for the three vertices of the triangle T_m^p or T_n^q, $\underline{r}^c$ is the centroid of the triangle T_m^p or T_n^q, and A is the area of T_m^p. $\underline{r}_m$ and $\underline{r}_n$ are the position vectors for the free vertex of the triangles T_m^p and T_n^q, respectively. We note that if the field point does not lie on the triangle T_n^q, i.e., $\underline{r} \notin T_n^q$, the result is $C_{mn}^{pq} = 0$. In (A12), the sign is positive when p and q are same and negative otherwise.

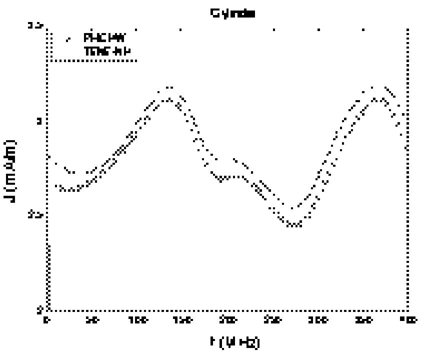

(a) Electric current

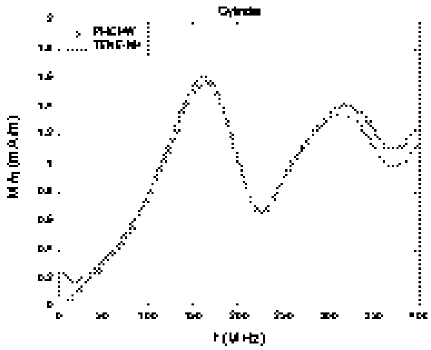

(b) Magnetic current

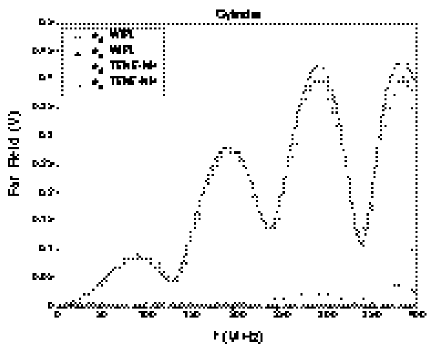

(c) Normalized far field

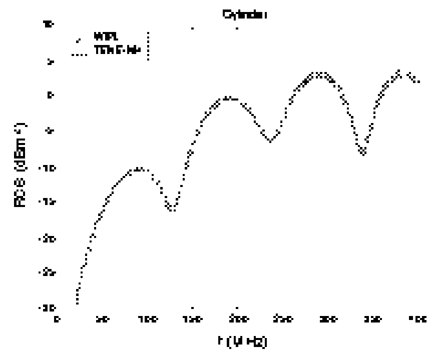

and (d) Monostatic RCS

Figure 37. TENE-NH results for a dielectric cylinder ($f_E = 1,\ g_E = 1,\ f_H = 0,\ g_H = 1$).

Using the summation operator, (77) is given by

$$C^f_{mn} = \frac{1}{2}\int_S \underline{f}_m(\underline{r}) \cdot \hat{n} \times \underline{f}_n(\underline{r}) dS = \sum_{p,q} \frac{1}{2}\int_S \underline{f}^p_m \cdot \hat{n} \times \underline{f}^q_n dS. \quad \text{(A13)}$$

By evaluating the element of (A13) analytically, the result is given by

$$\frac{1}{2}\int_S \underline{f}^p_m \cdot \hat{n} \times \underline{f}^q_n dS = \pm \frac{l_m l_n}{8A} \hat{n} \cdot [(\underline{r}_m - \underline{r}_n) \times \underline{r}^c - (\underline{r}_m \times \underline{r}_n)]. \quad \text{(A14)}$$

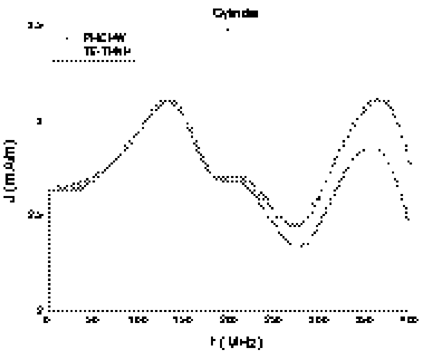

(a) Electric current

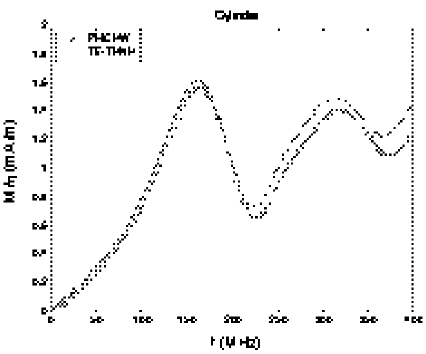

(b) Magnetic current

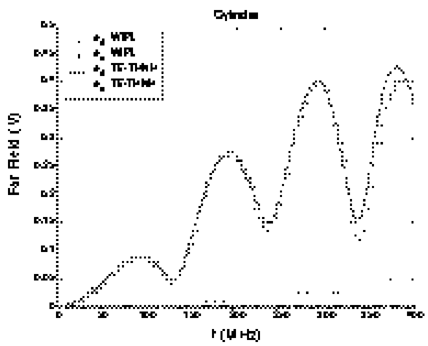

(c) Normalized far field

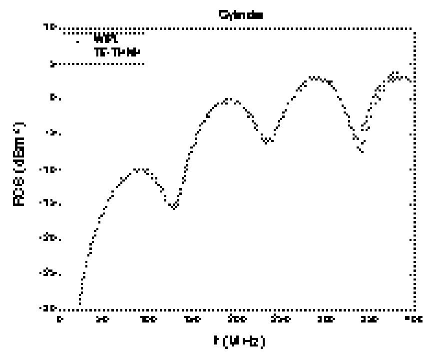

(d) Monostatic RCS

Figure 38. TE-THNH results for a dielectric cylinder ($f_E = 1,\ g_E = 0,\ f_H = -1,\ g_H = 1$).

By using a vector identity [8], (78) may be written as

$$C^g_{mn} = \frac{1}{2}\int_S \hat{n} \times \underline{f}_m(\underline{r}) \cdot \hat{n} \times \underline{f}_n(\underline{r}) dS = \sum_{p,q} \frac{1}{2}\int_S \underline{f}^p_m(\underline{r}) \cdot \underline{f}^q_n(\underline{r}) dS \quad \text{(A15)}$$

where the integral is same as in (A12).

A.4. Integrals (37), (51), (79), and (80)

By using the summation operator, we may write terms of (37) as

$$D^{pq}_{mn} = \frac{1}{4\pi}\int_S \underline{f}^p_m(\underline{r}) \cdot \int_S \hat{n}' \times \underline{f}^q_n(\underline{r}) \times \nabla' G(\underline{r}, \underline{r}') dS' dS \qquad \text{(A16)}$$

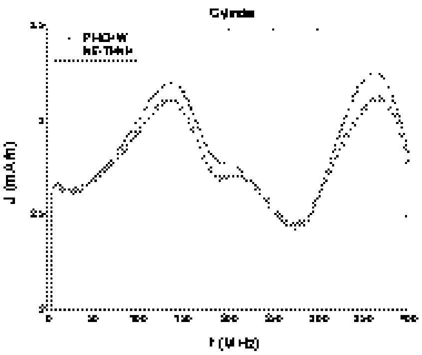

(a) Electric current

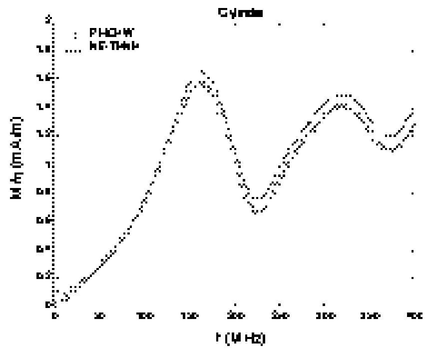

(b) Magnetic current

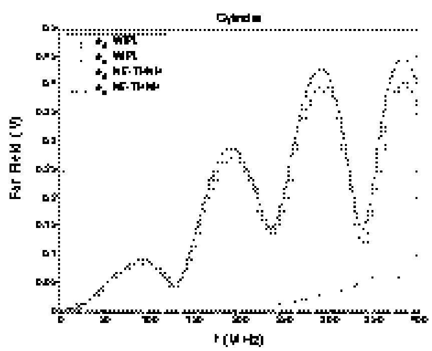

(c) Normalized far field

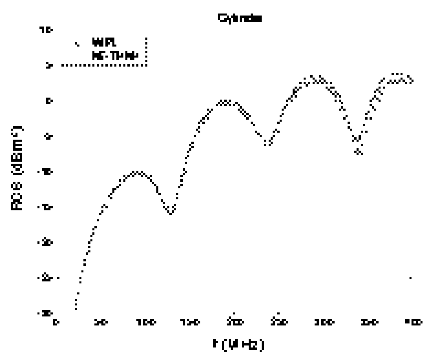

(d) Monostatic RCS

Figure 39. NE-THNH results for a dielectric cylinder ($f_E = 0,\ g_E = 1,\ f_H = -1,\ g_H = 1$).

where $\hat{n}'$ denotes the unit vector normal to the triangle T_n^q. Thus, substituting (17b) into (A16), we obtain

$$D_{mn}^{pq} = \frac{l_m l_n}{16\pi A_m^p A_n^q} \int_{T_m^p} \underline{\rho}_m^p \cdot \int_{T_n^q} (\hat{n}' \times \underline{\rho}_n^q) \times \underline{R}(1 + jkR) \frac{e^{-jkR}}{R^3} dS' dS. \tag{A17}$$

This integral may be computed using a Gaussian quadrature scheme over the unprimed and primed coordinates numerically. Other integrals of (51), (79), and (80) may be evaluated in a similar fashion.

A.5. Integrals (40), (46), (50), (54), (72), and (89)

We consider (40) for $v = 1$ and apply a centroid testing, yielding

$$\begin{aligned}\int_S \underline{f}_m(\underline{r}) \cdot \underline{E}^i(\underline{r}) dS &= \int_S \underline{f}_m^+(\underline{r}) \cdot \underline{E}^i(\underline{r}) dS + \int_S \underline{f}_m^-(\underline{r}) \cdot \underline{E}^i(\underline{r}) dS \\ &= \frac{l_m}{2}\{\underline{\rho}_m^{c+} \cdot \underline{E}^i(\underline{r}_m^{c+}) + \underline{\rho}_m^{c-} \cdot \underline{E}^i(\underline{r}_m^{c-})\}. \end{aligned} \tag{A18}$$

Other integrals may be evaluated in a similar fashion.

REFERENCES

1. Harrington, R. F., "Boundary integral formulations for homogeneous material bodies," *J. Electromagn. Waves Applicat.*, Vol. 3, No. 1, 1–15, 1989.
2. Umashankar, K., A. Taflove, and S. M. Rao, "Electromagnetic scattering by arbitrary shaped three-dimensional homogeneous lossy dielectric bodies," *IEEE Trans. Antennas Propagat.*, Vol. 34, No. 6, 758–766, June 1986.
3. Sarkar, T. K., S. M. Rao, and A. R. Djordjevic, "Electromagnetic scattering and radiation from finite microstrip structures," *IEEE Trans. Microwave Theory Technol.*, Vol. 38, No. 11, 1568–1575, Nov. 1990.
4. Rao, S. M., and D. R. Wilton, "E-field, H-field, and combined field solution for arbitrarily shaped three-dimensional dielectric bodies," *Electromagn.*, Vol. 10, 407–421, 1990.
5. Rao, S. M., C. C. Cha, R. L. Cravey, and D. L. Wilkes, "Electromagnetic scattering from arbitrary shaped conducting bodies coated with lossy materials of arbitrary thickness," *IEEE Trans. Antennas Propagat.*, Vol. 39, No. 5, 627–631, May 1991.
6. Sheng, X. Q., J. M. Jin, J. M. Song, W. C. Chew, and C. C. Lu, "Solution of combined-field integral equation using multilevel fast multipole algorithm for scattering by homogeneous bodies," *IEEE Trans. Antennas Propagat.*, Vol. 46, No. 11, 1718–1726, Nov. 1998.
7. Rao, S. M., D. R. Wilton, and A. W. Glisson, "Electromagnetic scattering by surfaces of arbitrary shape," *IEEE Trans. Antennas Propagat.*, Vol. 30, No. 5, 409–418, May 1982.
8. Harrington, R. F., *Time Harmonic Electromagnetics*, McGraw-Hill, New York, 1961.
9. Rao, S. M., "Electromagnetic scattering and radiation of arbitrarily-shaped surfaces by triangular patch modeling," Ph.D. Dissertation, Univ. Mississippi, Aug. 1980.

10. Kolundzija, B. M., J. S. Ognjanovic, and T. K. Sarkar, *WIPL-D Electromagnetic Modeling of Composite Metallic and Dielectric Structures, Software and User's Manual*, Artech House, Norwood, 2000.
11. Wilton, D. R., S. M. Rao, A. W. Glisson, D. H. Schaubert, O. M. Al-Bundak, and C. M. Butler, "Potential integrals for uniform and linear source distributions on polygonal and polyhedral domains," *IEEE Trans. Antennas Propagat.*, Vol. 32, No. 3, 276–281, March 1984.
12. Caorsi, S., D. Moreno, and F. Sidoti, "Theoretical and numerical treatment of surface integrals involving the free-space Green's function," *IEEE Trans. Antennas Propagat.*, Vol. 41, No. 9, 1296–1301, Sept. 1993.
13. Graglia, R. D., "On the numerical integration of the linear shape functions times the 3-D Green's function or its gradient on a plane triangle," *IEEE Trans. Antennas Propagat.*, Vol. 41, No. 10, 1448–1455, Oct. 1993.
14. Eibert, T. F., and V. Hansen, "On the calculation of potential integrals for linear source distributions on triangular domains," *IEEE Trans. Antennas Propagat.*, Vol. 43, No. 12, 1499–1502, Dec. 1995.